INFORMATION TO USERS

This manuscript has been reproduced from the microfilm master. UMI films the text directly from the original or copy submitted. Thus, some thesis and dissertation copies are in typewriter face, while others may be from any type of computer printer.

The quality of this reproduction is dependent upon the quality of the copy submitted. Broken or indistinct print, colored or poor quality illustrations and photographs, print bleedthrough, substandard margins, and improper alignment can adversely affect reproduction.

In the unlikely event that the author did not send UMI a complete manuscript and there are missing pages, these will be noted. Also, if unauthorized copyright material had to be removed, a note will indicate the deletion.

Oversize materials (e.g., maps, drawings, charts) are reproduced by sectioning the original, beginning at the upper left-hand corner and continuing from left to right in equal sections with small overlaps. Each original is also photographed in one exposure and is included in reduced form at the back of the book.

Photographs included in the original manuscript have been reproduced xerographically in this copy. Higher quality 6" x 9" black and white photographic prints are available for any photographs or illustrations appearing in this copy for an additional charge. Contact UMI directly to order.

UMI

A Bell & Howell Information Company
300 North Zeeb Road, Ann Arbor MI 48106-1346 USA
313/761-4700 800/521-0600

Université d'Ottawa • University of Ottawa

The Nature of the Metal-Insulator Transition in SiGe Quantum Wells

University of Ottawa & National Research Council Canada

in partial fulfillment of the requirements of a Master's Degree in Physics

by

© Jennifer Lam

May, 1997

National Library of Canada

Acquisitions and Bibliographic Services

395 Wellington Street
Ottawa ON K1A 0N4
Canada

Bibliothèque nationale du Canada

Acquisitions et services bibliographiques

395, rue Wellington
Ottawa ON K1A 0N4
Canada

Your file Votre référence

Our file Notre référence

The author has granted a non-exclusive licence allowing the National Library of Canada to reproduce, loan, distribute or sell copies of his/her thesis by any means and in any form or format, making this thesis available to interested persons.

L'auteur a accordé une licence non exclusive permettant à la Bibliothèque nationale du Canada de reproduire, prêter, distribuer ou vendre des copies de sa thèse de quelque manière et sous quelque forme que ce soit pour mettre des exemplaires de cette thèse à la disposition des personnes intéressées.

The author retains ownership of the copyright in his/her thesis. Neither the thesis nor substantial extracts from it may be printed or otherwise reproduced with the author's permission.

L'auteur conserve la propriété du droit d'auteur qui protège sa thèse. Ni la thèse ni des extraits substantiels de celle-ci ne doivent être imprimés ou autrement reproduits sans son autorisation.

0-612-20977-6

Canada

ABSTRACT

A study of the temperature dependence of the resistivity of gated SiGe quantum well structures has revealed a metal-insulator transition as a function of carrier density at zero magnetic field. Although early scaling theories (Abrahams et al., 1979) have argued against the existence of a metal-insulator transition at zero temperature in infinite 2D and 1D systems, more recent theoretical results using a random set of two-dimensional point potentials have shown that such a transition is allowed in two dimensions (Az'bel, 1992). Mounting experimental evidence for such a transition in 2D systems with short range scattering has accumulated in both semiconducting and superconducting structures (Kravchenko et al, 1995, and others).

Pseudomorphic, CVD-grown p-type $Si/Si_{0.87}Ge_{0.13}/Si$ quantum wells of various widths (65-200 Å) have been studied. The samples were gated using a Ti-Au Schottky gate to allow for carrier density variation. Measurement of the transport to quantum lifetime ratio indicates that the transport is dominated by short range scattering. In the temperature range from 400 mK - 4.2 K, the temperature dependence shows a transition from a metallic phase in the high density regime to an insulating phase in the low density regime with a transition boundary close to 2.2×10^{11} cm^{-2}. The scaling properties of the observed metal - insulator transition will be discussed, and compared to previous scaling results from silicon MOSFETs.

Below 400 mK, the onset of another transition is accompanied by a sharp drop in resistivity with temperature followed by a monotonic decrease in resistivity below 115 mK. The phase diagram was explored using temperature and density dependences of the current-voltage characteristics.

To my husband

STATEMENT OF ORIGINALITY

To the best of my knowledge, the work that I have completed at the National Research Council of Canada under the supervision of Dr. Marie D'Iorio is unique. Literature searches have revealed no publications to date addressing the metal-insulator transition in silicon germanium quantum wells at zero magnetic field other than those we have written.

The work which I have undertaken at the National Research Council during the course of my degree has included planning and carrying out transport measurements on silicon germanium quantum well samples using an Oxford top-loading dilution refrigerator and 15 T magnet. This included basic characterization of samples at 1.2 K followed by extensive measurements in the dilution refrigerator probing the temperature and carrier density dependence of the resistivity. The data was mainly analysed using Microcal Origin.

I have also assisted in the diagnosis and repair of cryogenic leaks, and contributed to maintaining the low temperature facility in good working order.

RELEVANT PUBLICATIONS AND CONFERENCE PRESENTATIONS

J. Lam, M. D'Iorio, D. Brown, D. Stewart, and H. Lafontaine; *Evidence for a Coulomb Gap in the Temperature Dependence of the Insulating Phase in a Si/SiGe 2D Hole Gas*, (in preparation).

M. D'Iorio, J. Lam, D. Brown, D. Stewart, and H. Lafontaine; *The Nature of the Insulating Phase in a p-type SiGe Quantum Well*, (in preparation).

M. D'Iorio, D. Brown, J. Lam, D. Stewart, S. Deblois and H. Lafontaine, *Evidence for a Metal-Insulator Transition at B=0 in Si/SiGe/Si Quantum Wells*, Superlattices and Microstructures, (accepted July 15, 1996).

M. D'Iorio, D.Brown, J. Lam, D. Stewart, S. Deblois, and H. Lafontaine; *Study of the Metal-Insulator Transition at B=0 in* $Si/Si_{0.87}Ge_{0.13}/Si$ *Quantum Wells*, June 1996, Annual CAP Congress.

ACKNOWLEDGEMENTS

I am greatly indebted to Dr. Marie D'Iorio, my supervisor at the National Research Council, for her guidance and support, and to her laboratory technician Don Brown for his immense patience. The samples used were fabricated by Hugues Lafontaine of the National Research Council, and the gates deposited by Duncan Stewart (a previous student). Calculations based on the sample parameters were undertaken by Louis Rego of the National Research Council.

Throughout my degree I have benefitted greatly from the supportive academic atmosphere at the University of Ottawa, and contact with my co-supervisor Dr. Emery Fortin.

TABLE OF CONTENTS

Abstract — i

Statement of Originality — iii

Relevant Publications and Conference Presentations — iv

Acknowledgements — v

Table of Contents — vi

List of Figures — vii

Introduction — 1

Semiconductor Quantum Structures — 4
- Energy Levels — 5
- Density of States — 8
- Magnetic Field Effects — 9
- Shubnikov-de Haas Effect — 11
- Transport Theory — 12
- Quantum Transport — 15
- Metal-Insulator Transitions — 22
- Silicon Germanium Structures — 26
- SiGe Valence Band Structure — 29

Samples and Experimental Details — 32
- UHV-CVD — 32
- Schottky Gates — 34
- Refrigeration — 37
- Magnet — 39
- Measurements — 39
- Sample Design and Characterization — 42

Results and Discussion — 50
- Coulomb Gap — 52
- Scaling — 54
- Low Temperatures — 56
- Threshold Field — 58

Conclusions — 66

References — 69

LIST OF FIGURES

Figure 1: Two-dimensional electron gas formation 4
Figure 2: The potential well formed by a symmetrically doped quantum well structure 6
Figure 3: Energy levels in a square well 7
Figure 4: Electron density of states, two and three dimensions 8
Figure 5: Density of states in a magnetic field 9
Figure 6: Silicon MOSFET measurements of resistivity vs. temperature 14
Figure 7: Quantum Hall Effect example 17
Figure 8: Parameters of interest for Wigner crystallization 19
Figure 9: Phase diagram of a two-dimensional electron system 21
Figure 10: Growth of 20% lattice mismatched epitaxial layers in a square lattice 27
Figure 11: Strained layer thicknesses possible for ratios of $Si_{1-x}Ge_x$ 29
Figure 12: Si/SiGe interface barriers 29
Figure 13: Heavy and light hole energy band splitting 30
Figure 14: Energy levels of a 65 Å $Si_{0.87}Ge_{0.13}$ *quantum well* 31
Figure 15: CVD 124, 200 Å $Si_{0.87}Ge_{0.13}$ *quantum well design* 32
Figure 16: CVD 32J/32K, 65 Å $Si_{0.87}Ge_{0.13}$ *quantum well design* 34
Figure 17: Hall Bar Configuration 34
Figure 18: Energy Bands of a Schottky Barrier 36
Figure 19: Block Diagram of System 39
Figure 20: Sample Measurement Circuit 40
Figure 21: Gate Leakage Circuit 41
Figure 22: Mobility and carrier density as a function of temperature 42
Figure 23: CVD 124, Hall and longitudinal resistivities 43
Figure 24: CVD 124, Landau level splitting 43
Figure 25: A Dingle plot for sample CVD 124 44
Figure 26: Gate Leakage Results, all samples 46
Figure 27: Sample 32K, resistivity for different carrier densities at 25 mK 48
Figure 28: Sample Characterization Results 48
Figure 29: ρ_{xx} *vs. Temperature as a function of well width* 49
Figure 30: Temperature dependence of resistivity, sample 32K 51
Figure 31: Sample 32K, Fits to insulating curves 53
Figure 32: Scaling of T_o *for sample 32K* 55
Figure 33: Low temperatures, sample 32K 56
Figure 34: Longitudinal Resistivity Against Carrier Density 57
Figure 35: Current-Voltage Measurements 59
Figure 36: Threshold field results, sample 32K 60

INTRODUCTION

As sample growth techniques have improved it has become possible to grow semiconductor heterojunctions of very high mobilities. The study of the quasi two-dimensional electron gas which forms in such structures has revealed an unexpected richness of 2D carrier behavior with quantum effects not observable in three-dimensional systems.

Recent measurements of high mobility silicon MOSFETs (metal-oxide-semiconductor field effect transistors) have provided evidence for the formation of a Wigner solid at B=0 below a critical temperature and carrier density. The manifestation of the Wigner solid is through the onset of an insulating phase. At zero field there is a metal-insulator transition as a function of temperature showing universal scaling, and the presence of Coulomb gap behavior in both the metallic and insulating phases. Important parameters of the silicon MOSFETs relating to the observed zero field behavior are a large effective mass (m^*), a low dielectric constant (κ), large spin-orbit coupling, and population of two valleys. These factors are believed to enhance the formation of the Wigner solid as the ordering Coulomb interaction competes with the disordering zero point oscillation energy.

Other semiconductor heterojunction systems should exhibit similar features at zero field, given a combination of the same parameters. Finding such a combination, however, is not straightforward. None of the easy to grow III-V

semiconductor junctions satisfy the general criteria of high effective mass and low dielectric constant, and only in recent years has the growth of silicon-silicon germanium devices yielded high mobility structures. Using UHV-CVD (ultra-high vacuum chemical vapour deposition) techniques, silicon germanium quantum wells have now been fabricated which are comparable in quality to III-V structures. The p-type heterojunctions have a high effective mass, and the dielectric constant is slightly lower than that of III-V structures. As valence band mixing effects and spin orbit coupling lead to a replacement of spin by parity as a good quantum number, the 2D hole gas behaves as a coupled gas in a double well.

These promising features of Si/SiGe quantum wells prompted an investigation of zero field behavior in the hope that results might prove similar to those for silicon MOSFETs, and provide a clearer picture of Wigner crystallization. Previous results at field had shown that reentrant metal-insulator transitions were present in silicon germanium structures, occurring at half-filled Landau levels reentrantly with the quantum Hall effect as had been observed in silicon MOSFETs. This study undertakes a search for signatures of the Wigner crystal and a full characterization of the metal-insulator transition, both at zero magnetic field.

Presented here are the results of this investigation, beginning with a review of the theory of semiconductor heterostructures and quantum transport (chapter one). A full description of the samples, apparatus, and measurement techniques follows in chapter two along with basic characterization of the quantum wells. Finally evidence of a true metal-insulator transition is presented, to-

gether with measurements consistent with the existence of a Wigner solid at zero field and the onset of another transition to a different phase - possibly that of a binary solid/gas phase - below 400 mK (chapter three). A summary of the results appears in the conclusion.

SEMICONDUCTOR QUANTUM STRUCTURES

A two-dimensional electron gas (2DEG) is formed at any semiconductor interface where the motion of the charge carriers is free in two spatial dimensions but confined in the third. Spatial variations of the potential energy of the conduction and valence bands result in the formation of a potential well where carriers are confined. The early work on 2D electron systems was done on Si-MOSFETs which are easily manufactured and provide a wide variation of carrier densities by the variation of bias applied to the gate. Because of the poor mobility of Si-MOSFETs, the focus of work on 2D systems switched to semiconductor-semiconductor interfaces as sophisticated growth techniques such as molecular beam epitaxy allowed for atomic scale control of the deposition.

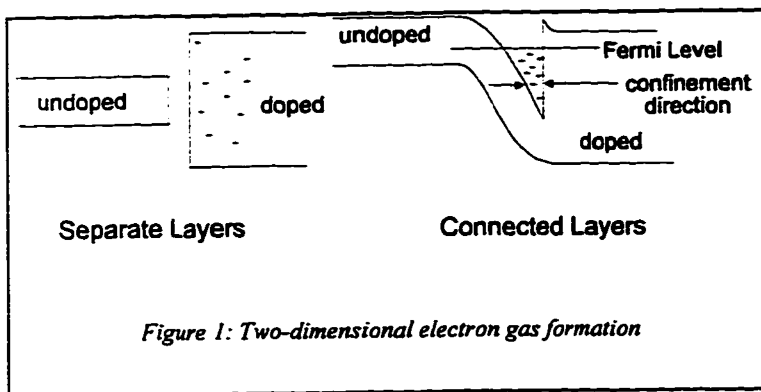

Figure 1: Two-dimensional electron gas formation

At the interface between two semiconductors, the difference in electron affinities results in offsets in the conduction and valence bands. When the work functions of the materials differ, charge transfer occurs across the interface to maintain a constant Fermi level. When the transfer of charge is sufficiently high, the band bending becomes strong enough to confine carriers in the resulting well. Whereas in Si-MOSFETs the carrier density is varied by the applied bias

on the gate, the carrier density in semiconductor heterojunctions is determined by doping the large bandgap material. Modulation doping refers to the separation of the dopant layer from the well by an undoped buffer layer. The isolation of the charge carriers from the long range impurity potential of the dopant atoms leads to increased mobility in heterojunctions. An insulating layer such as an oxide adjacent to a semiconductor has the same net effect, but band bending is achieved using a metal 'gate' layer on the insulator. The Fermi level and band bending involved in confining electrons are depicted in Figure 1, where the interface potential well resides on the side of the semiconductor with the smaller bandgap.

Energy Levels

The potential well formed by the difference in bandgap of the layers of a quantum well may be approximated by a triangular potential well with the barrier height larger than the well width. The effect of sandwiching a small bandgap material between two layers of a larger bandgap material such that both interfaces confine carriers combines two triangular wells, forming an almost square well as shown in Figure 2. In wells as wide as 400Å or more the confined carriers remain isolated in two separate pockets as studied by Guldner et al. (1993). For narrow well widths the curvature of the bottom of the well is negligible, and the carriers are confined in the square quantum well.

When carriers are confined to a spatial extent z comparable to the de Broglie wavelength (~100 Å), as is the case for electrons at the Fermi level in semiconductor heterostructures, the electronic states can be described by the Schrödinger equation in the effective mass approximation. For an infinitely deep well, the model of a particle in a box may be applied:

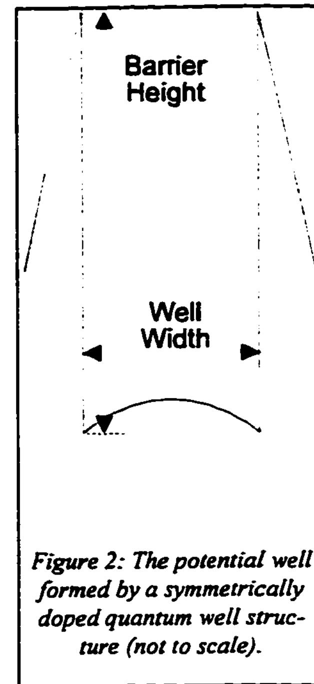

Figure 2: The potential well formed by a symmetrically doped quantum well structure (not to scale).

$$1\text{-}1 \quad -\left(\frac{\hbar^2}{2m^*}\right)\frac{\partial^2\psi}{\partial z^2} = (E - V)\psi$$

where ψ is the electron wave function, z is the direction of the well width L, and E is the electron energy level. The solutions are plane waves with eigenenergies given by:

$$1\text{-}2 \quad E_n = \frac{\hbar^2}{2m^*}\left(\frac{(n+1)\pi}{L}\right)^2; \quad n=0,1,2,\ldots \quad \text{and} \quad \psi_n(z) = A\sin\frac{n\pi z}{L}$$

where
$$V(z) = \begin{cases} 0, & 0 \le z \le L \\ \infty, & z \le 0, z \ge L \end{cases}$$

The electron wave function ψ is restricted to the well width L by the infinite potential barriers on either side, as shown in Figure 3. When the finite potential barrier height is introduced the electron wave function is no longer constrained to the width of the well but may extend into the walls of the well as shown in the fig-

ure. In this case z=0 is taken to be the center of the well, and the energy level and wave function solutions are given for odd solutions by:

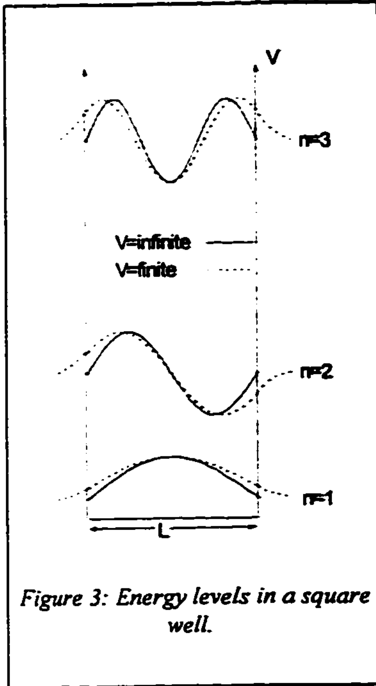

Figure 3: Energy levels in a square well.

1-3A $$E_n = -\frac{\hbar^2\kappa^2}{2m_B^*}$$ and

$$\psi(z) = \begin{cases} e^{k_2 z} B\cos\left(\frac{k_1 L}{2}\right) e^{k_2 L/2} \\ B\cos(k_1 z) \\ e^{-k_2 z} B\cos\left(\frac{k_1 L}{2}\right) e^{k_2 L/2} \end{cases} \quad \text{where} \quad \begin{cases} z < -\frac{L}{2} \\ -\frac{L}{2} < z < \frac{L}{2} \\ z > \frac{L}{2} \end{cases}$$

or for even solutions, by:

1-3B $$E_n = \frac{\hbar^2\kappa^2}{2m_A^*} - V$$ and

$$\psi(z) = \begin{cases} -e^{k_2 z} A\sin\left(\frac{k_1 L}{2}\right) e^{k_2 L/2} \\ A\sin(k_1 z) \\ e^{-k_2 z} A\sin\left(\frac{k_1 L}{2}\right) e^{k_2 L/2} \end{cases} \quad \text{where} \quad \begin{cases} z < -\frac{L}{2} \\ -\frac{L}{2} < z < \frac{L}{2} \\ z > \frac{L}{2} \end{cases}$$

Thus, once the electron wave function passes out of the potential well it decays exponentially while inside the well it retains a shape similar to that for infinite barriers.

Density of States

For a three-dimensional free electron gas, the density of states up to and including those of energy E is given by:

$$D(E) = \frac{1}{2\pi^2}\left(\frac{2m^*}{\hbar^2}\right)^{3/2} E^{1/2} \qquad (1\text{-}4)$$

where m^* is the effective electron mass.

The density of states for a two-dimensional quantum well differs from the three-dimensional value for an equivalent layer thickness in that the former always has a finite value while the latter tends towards zero at the bottom energy level. The density of states per energy subband for a two-dimensional quantum well as shown with the comparable three-dimensional model in Figure 4, is given by:

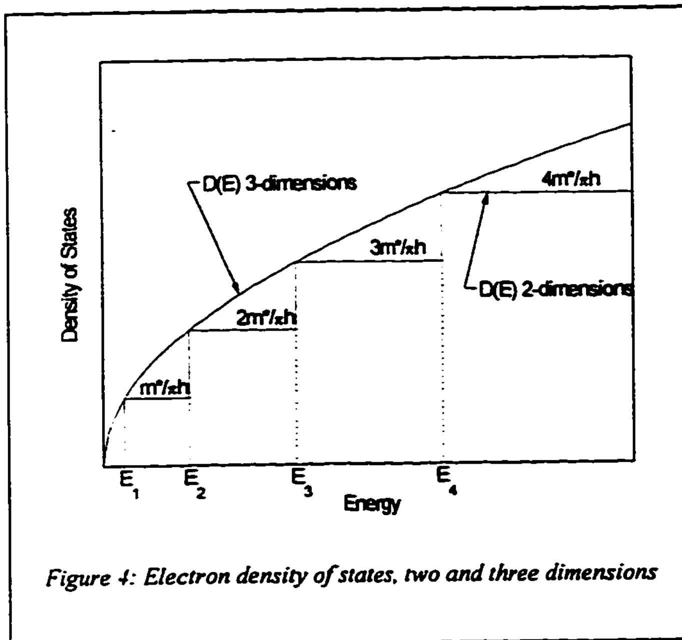

Figure 4: Electron density of states, two and three dimensions

$$D(E_n) = \frac{m^* n}{\pi \cdot \hbar^2} \qquad (1\text{-}5)$$

Thermal broadening results in an oscillatory density of states with a Gaussian profile causing some predictable deviation from the ideal density of states shown, where instantaneous changes in the density of states become gradual and the sharp corners shown in Figure 4 round off.

Magnetic Field Effects

When a magnetic field is applied along the z direction and the motion of the carriers is limited to the xy plane at the interface, the eigenenergies of the Hamiltonian become:

1-6 $$E_{n,i} = \left(n + \frac{1}{2}\right)\hbar\omega_c + E_i$$ where n is the Landau level index and i is the index of quantization energy level. The two-dimensional density of states for each subband E_i is a set of delta functions separated by the cyclotron energy:

1-7 $$D_{2D}(E) = \frac{2EB}{h}\delta(E - E_{n,i})$$

This is illustrated in Figure 5.

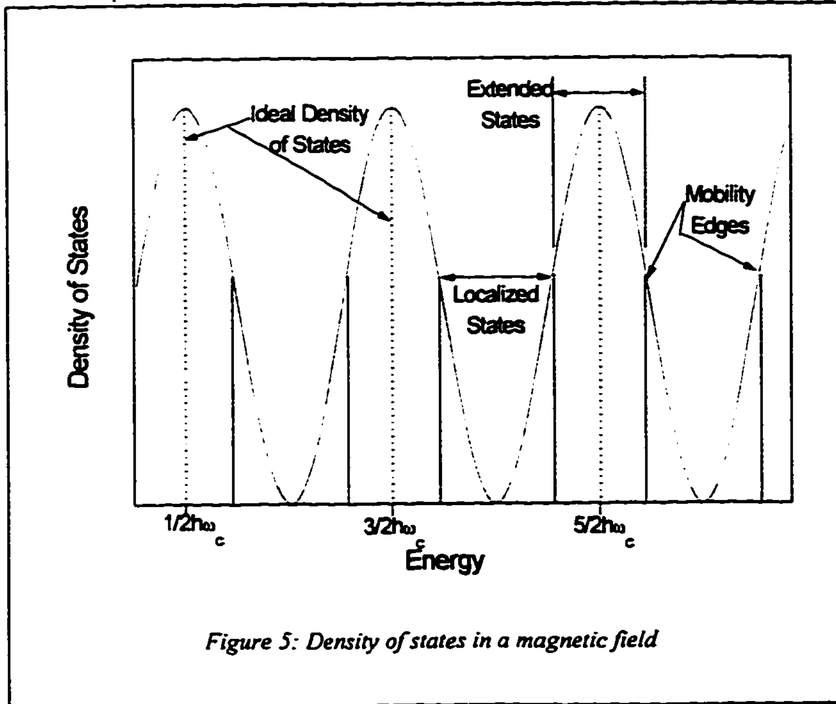

Figure 5: Density of states in a magnetic field

In a strong magnetic field, the spin degeneracy of the Landau levels is lifted. This leads to:

1-8 $$E_{i,n,s} = E_i + \left(n + \frac{1}{2}\right)\hbar\omega_c + sg^{*}\mu_B B$$

where $s=\pm 1/2$ for two spin orientations, g^* is the Landé factor, $\mu_B = \frac{e\hbar}{g_o m_o}$ is the Bohr magneton for the free electron mass m_0 and free g factor $g_o=2$.

The density of states is further split due to spin effects with peaks separated by $2sg^*\mu_B B$, where the spin splitting is usually small compared to the cyclotron energy. When the band structure is such that degenerate valleys can be populated, a further valley splitting will occur.

Interactions with impurity and defect potentials in the material as well as with phonons will lead to a broadening of the Landau levels which will smooth the singularities in the density of states. A lifetime τ is defined such that the width at half maxima of a Landau level is $\Gamma = \hbar/\tau$. Energy levels become distinct when the broadening is less than the cyclotron energy ($\hbar\omega_c$) separating them:

1-9 $$\Gamma < \hbar\omega_c \text{ or } \omega\tau = \mu B > 1$$ where μ is the mobility.

At low temperature, carriers in the tail of the Landau levels are localized and do not participate in conduction, whereas a band of extended states exists near the center of the Landau levels where electrons can carry current. The mobility edge separates the extended and localized states. In the limit of short range perturbing potential, the level broadening varies with magnetic field as $B^{1/2}$:

1-10 $$\Gamma = \left(\frac{2}{\pi}\frac{\hbar^2\omega}{\tau}\right)^{1/2} = \left(\frac{2}{\pi}\frac{eB\hbar}{m^*\tau}\right)^{1/2}$$ and is sensitive to the position of the Fermi level.

Shubnikov-de Haas Effect

For metallic conduction only those electrons within kT of the Fermi surface contribute to the diffusion process. The transition probability from one state to another will be proportional to the density of states, and will therefore be a maximum when the Fermi level crosses a Landau level. A maximum in the resistivity will occur for magnetic field values such that:

1-11 $$E_F = \left(n+\frac{1}{2}\right)\hbar\omega_n = \left(n+\frac{1}{2}\right)\frac{\hbar eB_n}{m^*}$$ where n is the Landau level index, and spin splitting is ignored. At low temperatures, the oscillatory behavior of the resistivity is known as the "Shubnikov-de Haas effect". The oscillations are periodic in 1/B, and the carrier density may be obtained from the periodicity of the oscillations:

1-12 $$\Delta\left(\frac{1}{B}\right) = \frac{e}{\pi\hbar N_{2D}} = \frac{\hbar e}{m^* E_F}$$ where N_{2D} is the carrier density.

The number of sets of oscillations will correspond to the number of occupied levels in the well, and the periodicity of the oscillations at low magnetic field yields the carrier density. The oscillating function describing the Shubnikov-de Haas oscillations is given by:

1-13 $$\rho_{xx} = 4\rho_o R_s\left(\frac{\xi}{\sinh\xi}\right)\exp\left(-\frac{\pi}{\omega_c\tau}\right)\cos\left(\frac{2\pi E_F}{\hbar\omega_c}+\delta\right)$$ where R_s is a spin splitting term, $\xi = \frac{2\pi kT}{\hbar\omega_c}$ (where $\omega_c = \frac{eB}{m^*}$), E_F is the Fermi energy, and δ is a phase factor.

Transport Theory

Any physical impurities (ionized or neutral) or crystal dislocations in the quantum well layer will scatter carriers, as will the rough interfaces between the silicon buffer layers and the silicon germanium quantum well. Alloy scattering due to the fluctuations in composition resulting from the mixing of different kinds of atoms will also occur. The net result will be short range scattering in and around the quantum well region. In addition, long range scattering of carriers can occur due to impurities present in the doped layers (separated from the quantum well layer via buffers,) and other impurities, dislocations, and interfaces far from the quantum well layer.

As the sample temperature is decreased the main scattering mechanisms change; at room temperature scattering due to phonons shifting the atomic lattice is prevalent, while at liquid helium temperature the scatterers described above dominate. The low temperature dependence of scattering (and thus mobility) on physical imperfections and impurities allows the fabrication of higher

and higher mobility samples as growth techniques advance and higher purity devices may be made.

The advent of modulation doping has led to an increase in mobilities of 2D electron gases by two orders of magnitude. The mobility is not necessarily a good indicator of sample quality; the information which is sought is what type of scattering is taking place, where it is taking place, and what is responsible for it. Scattering can take place at large to moderate angles if the scatterers are close to the 2DEG. However, short angle scattering will take place when the ionized donor impurities are placed further away by the use of spacer layers. We wish to find the total scattering probability Q(θ), or "quantum" lifetime τ_q where:

1-14 $$\frac{1}{\tau_q} = \int_0^t Q(\theta) d\theta$$ and compare it to the transport lifetime:

1-15 $$\frac{1}{\tau_t} = \frac{e}{m^* \mu_t}, \text{ where } \mu_t = \frac{1}{n_s e \rho_{xx}(B=0)}$$

The quantum lifetime is determined experimentally from Dingle plots, using the expression for the amplitude of the Shubnikov-de Haas oscillations:

1-16 $$\Delta\rho_{xx} = 4\rho_o A \exp\left(-\frac{\pi}{\omega_c \tau_q}\right) \text{ where } A = \frac{\left(\frac{2\pi^2 kT}{\hbar\omega_c}\right)}{\sinh\left(\frac{2\pi^2 kT}{\hbar\omega_c}\right)}$$ is the thermal damping factor. The logarithm of the amplitude divided by the thermal damping factor plotted against 1/B will yield the slope $1/\tau_q$, with an intercept at 1/B=0 of ρ_o.

The ratio of the transport lifetime τ_t to the quantum lifetime τ_q:

1-17

$$\alpha = \frac{\tau_t}{\tau_q}$$

represents the scattering length scale. An α value in the order of ten is indicative of long range scattering while the order of one is indicative of short range scattering. Thus larger α values show improvement in sample quality, with fewer short range scatterers present. It is still possible to have very high quality samples with α=1, since the dominating scattering mechanism can vary with carrier density.

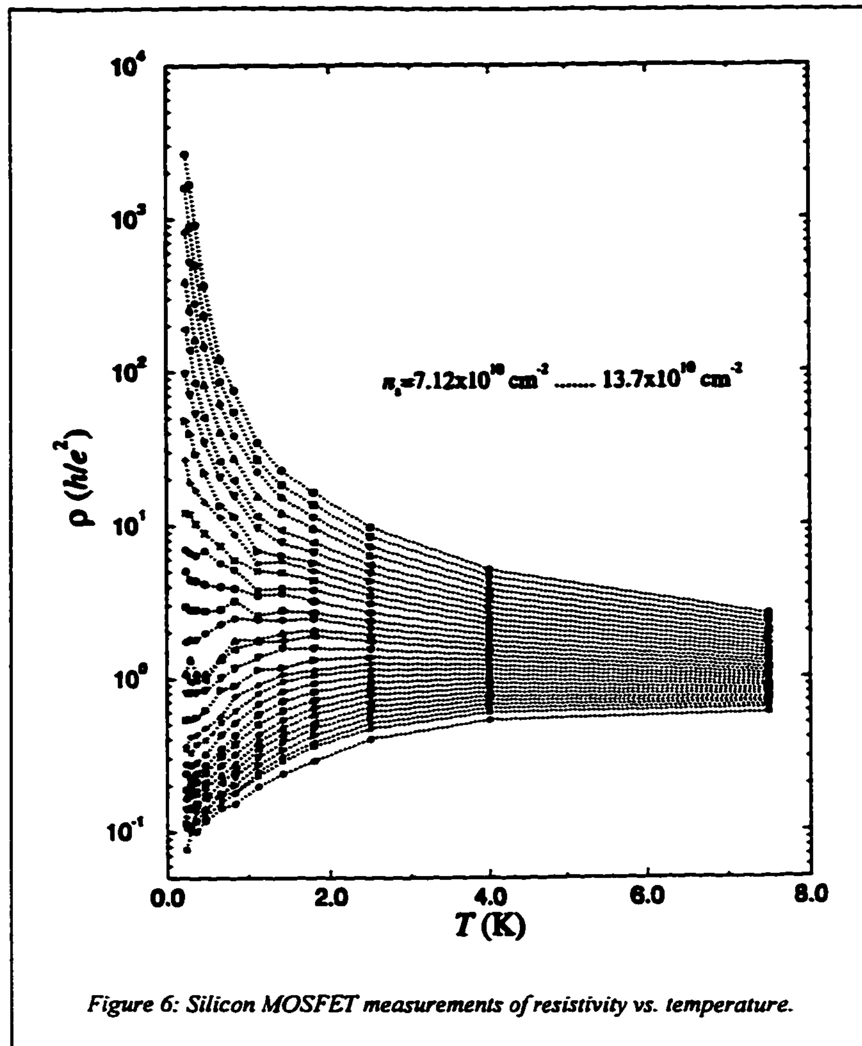

Figure 6: Silicon MOSFET measurements of resistivity vs. temperature.

At very low temperatures ordinary metals exhibit a dependence of resistance on the time between scattering events; as the frequency of phonons in the metal becomes less than the inverse scattering time, phonon scattering is rein-

troduced and the resistance saturates. The result is a minimum resistance, which cannot be decreased regardless of temperature. Such behavior is present in the metallic phase of most metal-insulator transitions while the insulating phase sees no such limits on its rising resistance. An exception has been measured in the resistance of silicon MOSFETs, where the metallic and insulating phases remain symmetric about the phase transition with an apparent absence of phonon scattering as shown in Figure 6.

Quantum Transport

When a magnetic field is applied perpendicular to a two-dimensional electron gas confined in the xy plane (of length L_x and width L_y), the conductance is given by :

1-18 $$\sigma_{xx} = \frac{\sigma_o}{1+(\omega_c\tau)^2} \quad \text{and} \quad \sigma_{xy} = \frac{\sigma_o\omega_c\tau}{1+(\omega_c\tau)^2} \quad \text{where} \quad \sigma_o = \frac{n_s e^2\tau}{m^*}$$

In the presence of strong magnetic fields at low temperatures ($\omega_c\tau >> 1$), the conductivity components approach the limits:

1-19 $$\sigma_{xx} = 0 \quad \text{and} \quad \sigma_{xy} = \frac{n_s e}{B}$$ and the current in the x direction is given by:

1-20 $$I_x = j_x L_y = \left(\frac{n_s e}{B}\right)(E_y L_y) = \left(\frac{n_s e}{B}\right)V_y$$ where j is the current density, L_x and L_y are the sample length and width, and E is the electric field due

to carrier motion. The Hall resistance is measured as the current flow along the sample and the voltage across the sample:

$$\rho_{xy} = \rho_H = \frac{V_y}{I_x} = \frac{B}{n_s e} \qquad (1\text{-}21)$$

In a strong magnetic field, Landau levels may be considered as either completely full or empty. The corresponding carrier density (at appropriate magnetic fields B_s, and any integer i) is:

$$n_s = \frac{ieB_s}{h} \qquad (1\text{-}22)$$

and the Hall resistance becomes:

$$\rho_H = \frac{h}{ie^2} \qquad (1\text{-}23)$$

where i=1,2,3, . . .

When these conditions are satisfied, no elastic collisions are possible in the same Landau level, and $\rho_{xx}=0$.

Hall measurements of thin quasi-two-dimensional layers at low temperatures exhibit such a material independent quantized Hall resistance, with flat plateaus appearing at integer multiples of h/e^2 as the magnetic field is varied. No geometric corrections are required provided that the sample length to width ratio is large (usually >5). The consistency of measurements has allowed the ratio of the two fundamental constants h and e to be determined to better than 1 part in 10^9. As shown in Figure 7 , the plateaus present in the increasing Hall resistance occur simultaneously with minima of the longitudinal resistance

(usually milliohms). The longitudinal resistance must be corrected for sample geometry, however, and is usually expressed as resistivity in Ohms per square (Ω/□), or resistance per unit area.

As the Fermi level is swept through the Landau levels of the quantum

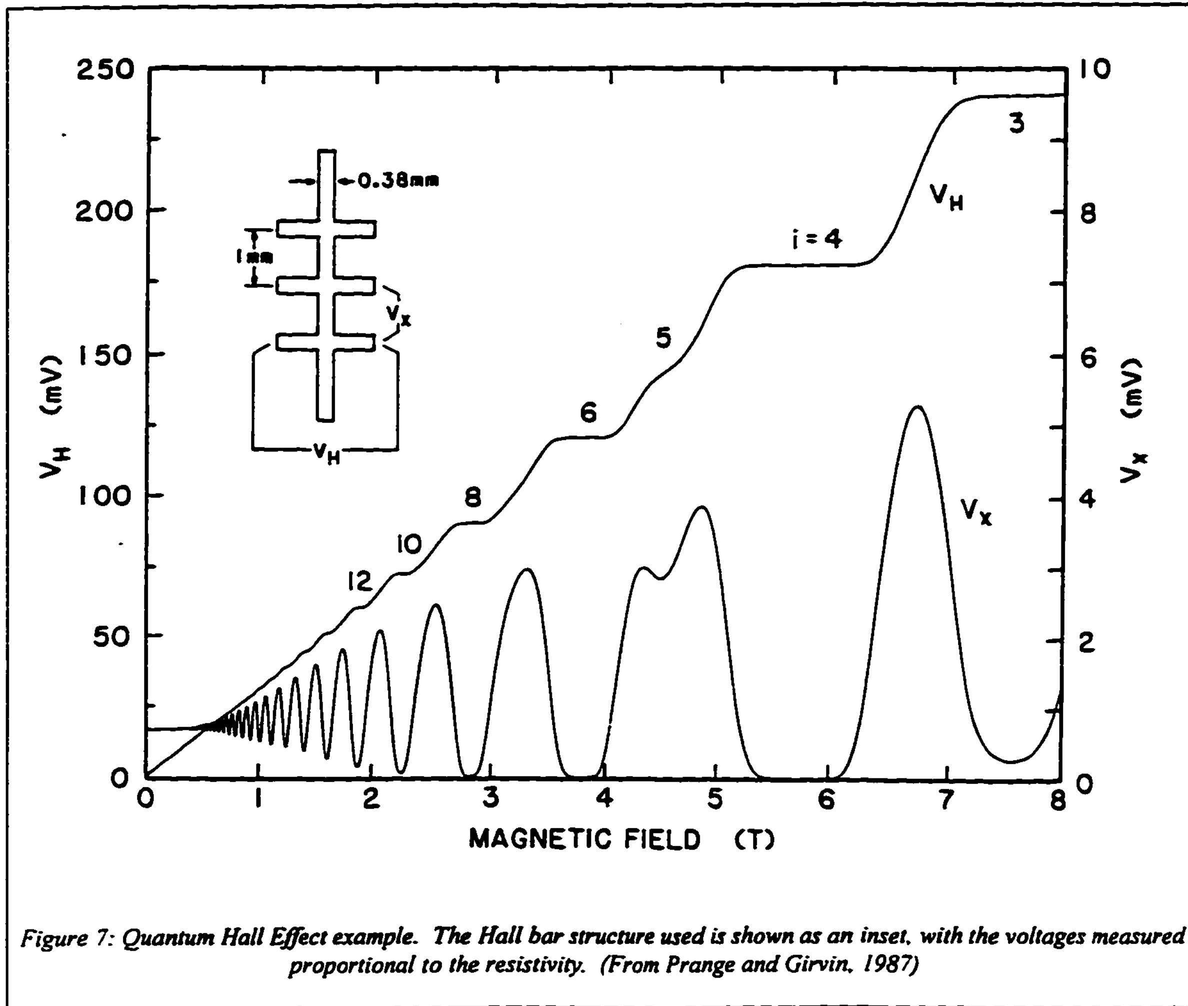

Figure 7: Quantum Hall Effect example. The Hall bar structure used is shown as an inset, with the voltages measured proportional to the resistivity. (From Prange and Girvin, 1987)

well, (by changing the magnetic field,) the highest energy level filled is either an extended state (conducting) or a localized state (non-conducting). Since localized states carry no current, a plateau in Hall resistance occurs while localized states are filling. Similarly the longitudinal resistance drops to near zero as the localized states fill. The finite temperatures used in experiments result in a small

longitudinal resistivity due to hopping processes despite the lack of current carrying states. The movement of the Fermi level through extended states appears as the transition from one plateau to the next in the Hall resistance, and as peaks in the longitudinal resistivity.

The fractional quantum Hall effect occurs in the extreme quantum limit where the lowest Landau level is partially occupied. The Hall resistance is a fractional multiple of h/e^2, while the longitudinal resistivity exhibits a minimum. Specifically, the fractions observed usually have an odd denominator and indicate a partially filled Landau level. The unlikely presence of partly filled Landau levels (in view of the quantization exhibited by the integer Hall effect) is explained through Coulomb interaction. As a transition occurs from an electron gas to a denser carrier state with many body interactions, (a carrier liquid,) Coulomb forces between electrons come into play. The coupling due to such forces creates a novel ground state with a fractional charge and characteristics of a quantum liquid. The integer and fractional Hall effects may be observed concurrently in high quality samples at low temperatures, as the magnetic field or carrier density is varied.

For dilute electron concentrations, it was proposed by Wigner in 1934 that a crystalline electron lattice would form at low temperatures when the Coulomb interaction became much larger than the disordering energy, in this case the thermal energy. Although the original prediction was made in reference to three-

dimensional metals, it has also been shown to apply to two-dimensional semiconductors (Crandall and Williams, 1971, and Chaplik, 1972).

Parameter	Si / SiGe	Si / SiO_2
electron effective mass m^*	0.44	0.19
dielectric constant $\langle \kappa \rangle$	12	7.7
Bohr radius $a_B = \frac{(4\pi\varepsilon_0)(\hbar^2\kappa)}{m^* e^2}$	14 Å	20 Å
interelectron spacing $a = \frac{1}{\sqrt{\pi \cdot n_s}}$	126 Å @n_s=2x10^{11} cm^{-2}	182 Å @n_s=9.6x10^{10} cm^{-2}
Wigner-Seitz radius $r_s = \frac{a}{a_B}$	9	10
Coulomb energy $E_{ee} = \frac{e^2}{\kappa \cdot a}$	112 K	90 K
Fermi energy $E_0 = \frac{\hbar^2}{m^* a^2}$	12.6K	7 K
critical concentration for quantum cold melting $n_q^{cm} = \frac{1}{\pi \cdot (r_c \cdot a_B)}$	(0.9-1.6) x 10[10] cm^{-2}	(0.4-0.7) x 10[10] cm^{-2}

Figure 8: Parameters of interest for Wigner crystalliation

There are two regimes for the formation of a Wigner solid, depending on whether the competing fluctuations are of thermal or quantum origin. In the classical regime the zero point oscillation energy is much smaller than the thermal energy k_BT:

1-24

$$k_BT_F = \frac{\hbar^2}{m^* a^2} << k_BT$$

where $a=(\pi n_s)^{-1/2}$ is the radius of the Wigner-Seitz cell, n_s is the carrier density, T_F is the Fermi temperature, and m^* is the effective mass. The ratio between the Coulomb correlation energy and the thermal disordering energy will be:

1-25 $$\Gamma = \frac{V_c}{k_B T} \text{ where } V_c \sim \frac{e^2}{\varepsilon(\pi n_s)^{-1/2}}$$ and the solid is expected

to form for large values of Γ. Evidence for a classical Wigner solid was found in a system of electrons on a thin film of helium. The "melting" of the solid occurred at Γ_m=127±3 (Rybalko et al. 1979, Grimes and Adams 1979, Mehrottra et al. 1982, Gallet et al.1984, and Deville 1988)

In the quantum regime, the temperature T is much lower than T_F, and the parameter of interest is the ratio of the Wigner-Seitz radius to the Bohr radius:

1-26 $$r_s = \frac{a}{a_B} = \frac{V_c}{k_B T_F} \text{ where } a_B = \frac{\hbar^2 \varepsilon}{e^2 m^*}$$

The electrons form a Wigner solid when the ratio r_s is large so that Coulomb correlations dominate. As the carrier density increases, the long range order vanishes because of increasing quantum fluctuations and the solid melts. The critical ratio for melting is r_s^W=37±5 (Ceperly 1978, and Tanator and Ceperly 1989).

Although Wigner's predictions were specifically made at zero magnetic field, it is possible to induce Wigner crystallization using a magnetic field to localize the electrons within a magnetic length $(\frac{\hbar}{eB})^{1/2}$ smaller than the Wigner Seitz radius a. The quantum fluctuations are quenched in this regime, and the overlap of electron variation is minimal.

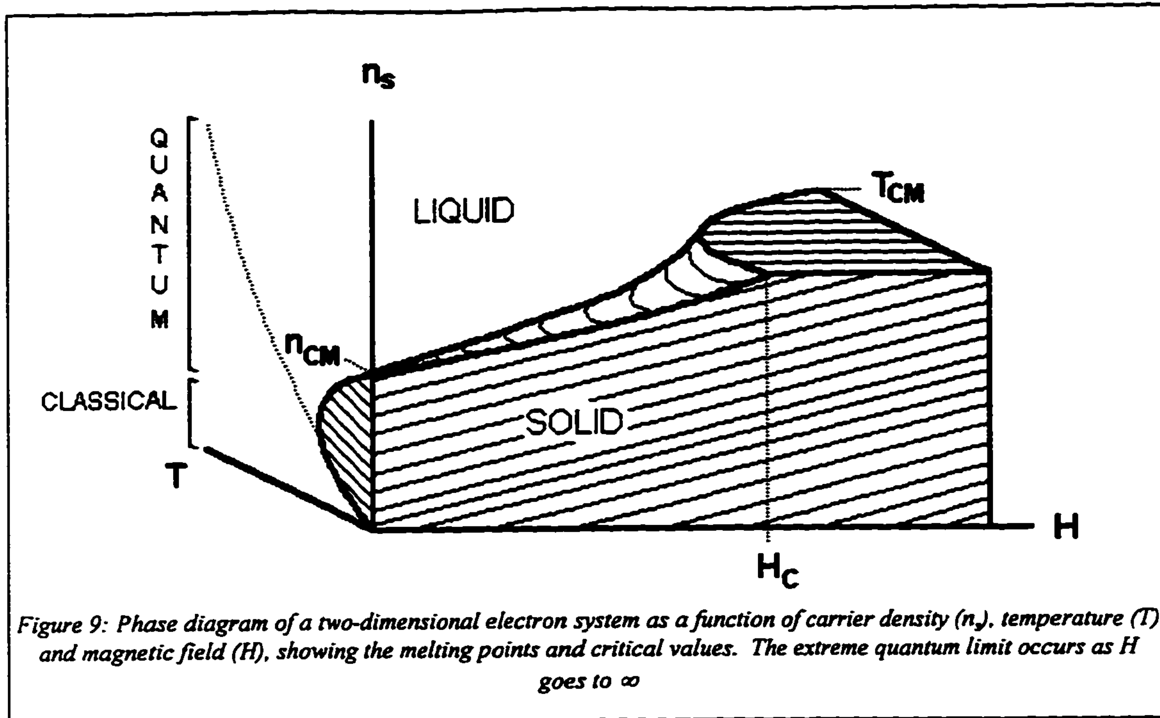

Figure 9: Phase diagram of a two-dimensional electron system as a function of carrier density (n_s), temperature (T) and magnetic field (H), showing the melting points and critical values. The extreme quantum limit occurs as H goes to ∞

Completing the electron phase diagram as is shown in Figure 9, the 2D electron gas should undergo two distinct transitions changing to a 'liquid' state and finally that of a 'solid' as a function of carrier density, temperature, and field. In the solid state, the repulsive inter-electron Coulomb force is expected to exceed the zero point oscillation energy of the electrons, leaving the lowest energy state one of evenly spaced carriers.

The presence of impurities results in a collection of crystallites: in analogy to charge density wave systems, the impurities can "pin" the crystal effectively blocking any conduction. A small threshold field is usually sufficient to overcome this pinning, allowing the crystal to "slide". A pinned lattice should exhibit non-linear current-voltage characteristics from which threshold values of voltage or field for crystal formation may be determined. The linear region represents the

pinned electron solid, while the wings are the sliding electron solid. The 'insulating' behavior of a Wigner solid is not a single-particle localization phenomenon due to disorder, but a collective excitation of the solid where electrons localized as a lattice cannot carry current. There is an intermediate phase between the electron gas or liquid and the Wigner solid, known as the Wigner glass. This would correspond to an 'amorphous' solid in systems with substantial disorder.

Experimental evidence for a Wigner solid exists near filling factors 1/5 and 2/7 in n-type heterojunctions, and 1/3 in p-type heterojunctions (Santos et al. 1992). Photoluminescence experiments have also indicated that the lattice has hexagonal symmetry (Kukushkin et al. 1994) as predicted by Wigner. The only material system which shows the typical signature of Wigner crystallization at zero magnetic field in the quantum limit is that of high mobility silicon MOSFETs.

Metal-Insulator Transitions

There are several theories describing metal-insulator transitions in three-dimensions based on the localization of electron wave functions, one initiated by Anderson, one by Mott, and one by Lifshitz (Shklovskii and Efros, 1984). While all three theories describe the same transitional result, they make different assumptions both about the structure of the materials involved, and the level of carrier interaction taking place throughout the transition.

Mott's model is based on regularly spaced impurities creating a lattice with a period much larger than that of the host lattice. The electrons of the impurity lattice form an energy band of allowed energy levels, with a gap appearing due to the carrier interaction energy present when two electrons occupy the same site. As the period of the impurity lattice decreases, the energy levels broaden and the size of the forbidden gap decreases. When the forbidden energy gap disappears, the transition from an insulator to a metal occurs with the formation of a single contiguous energy band.

The model proposed by Anderson assumes a disordered system in that each impurity has a different set of electron energy levels, resulting in a random overall distribution. Nearby impurity centers with equivalent energy levels form energy bands which extend throughout the host lattice. As the impurity concentration decreases, each impurity is less likely to be close to others with the same energy levels. At some critical concentration the impurities become localized due to their energy variation, and the Anderson transition from a metal to an insulator occurs. Lifshitz proposed a model similar to that of Anderson, but with variation in impurity location instead of energy levels. Once again the electrons are localized at low concentrations, only forming an extended energy band once some critical concentration is reached.

The main differences between the Mott transition and those of Anderson and Lifshitz are the roles of disorder and carrier interaction in each. The Mott

transition is based on carrier interactions and requires no disorder whatsoever. Anderson and Lifshitz transitions, on the other hand, are based on a single particle view with no carrier interaction, but do require the presence of disorder for the transition to occur. Most often discussed are the Mott and Anderson models, combined to form the more realistic Mott-Anderson transition of a disordered system with electron interactions. The insulating states of the transitions are known as Mott and Anderson insulators, with both the longitudinal and Hall resistivities of the sample tending to infinity as the temperature decreases to zero in both models.

The degree of carrier interaction occurring in a quantum well system may be determined experimentally based on the dependence of longitudinal resistivity on temperature. When Coulomb interactions are the dominant carrier mechanism, the resistivity is described by:

1-27 $$\rho_{xx} = A\exp\left(\frac{T_o}{T}\right)^{1/2}$$ where T_0 is a temperature dependent constant and A is a temperature independent constant. A similar temperature dependence is shown when variable range hopping is occurring, but with an exponential power of 1/3 instead of 1/2, representing minimal carrier interaction.

The transition models of Mott, Anderson, and Lifshitz discussed above are all based on three-dimensional electron systems, not the quasi-two-dimensional carrier layer present in quantum wells. Early predictions made by Abrahams et

al. (1979) claimed that a true metallic phase could not exist in an infinite two-dimensional system at zero magnetic field where electron states were always localized. Experimentally this was clearly not the case for semiconductor heterostructures, where ρ_{xy} was zero at zero field and ρ_{xx} had a finite value, usually 2 kΩ/□. A metal-insulator transition which scaled as a function of a universal parameter was revealed in thin superconducting Bi films and later in GaAs/AlGaAs low mobility structures and very high mobility MOSFETs. Some doubt was cast on the long-standing theory, and Az'bel (1992) proposed that extended states could indeed exist in some circumstances. Specifically, it was shown that a model of random two-dimensional point potentials is localized under the same conditions as a three dimensional system, that is for Fermi energies less than a critical energy E_c. The disparity between the two theories seems to hinge on the range of the scattering centers employed in the two models; while Az'bel's theory is consistent with short range scattering dominating the system, Anderson at al. fail to account for short range effects. Recent measurements of silicon MOSFETs with short range scatterers have supported the inclusion of scattering range in models of the two-dimensional metal-insulator transition. (Kravchenko at al., 1995)

A different insulating state has also been predicted specifically for two-dimensional electron systems, and has been observed at high magnetic fields near certain fractional filling factors and at half filled Landau levels 5/2 and 3/2. The Hall insulator has a longitudinal resistivity which tends towards infinity as

temperature goes to zero, but a Hall resistivity which stabilizes and remains finite, close to the classically expected value of $\rho_{xy} = \frac{B}{n_s e}$. As the carrier density n_s is decreased, the Hall insulating phase appears for additional filling factors, becoming more prevalent. The Hall insulator is a theoretical construct to account for experimental evidence associated with the formation of a Wigner solid.

A true phase transition exhibits sample independent scaling based on a single parameter representing some aspect of correlation throughout the system. An appropriate correlation length may refer to spin fluctuations, charge density waves, or any other variable of relevance to the physical system in question. In our case a localization length ξ will be examined as the metal-insulator transition is approached from both the metallic and insulating directions, and the carrier density is varied. For a true transition the following relation is expected to hold:

1-21 $$\xi = \left| \frac{n_c}{n_s - n_c} \right|^{-\frac{1}{\beta}}$$ where n_c is the critical carrier density of the transition, n_s is the varying carrier density, and $1/\beta=0.6$ (Shklovskii and Efros, 1984) is the critical exponent of the localization length (usually denoted ν, but renamed here to avoid confusion).

Silicon Germanium Structures

The growth of alloys of silicon and other lattice matched semiconductors allows detailed 'bandgap engineering' of the silicon/alloy heterostructures which may then be fabricated; the flexibility introduced by an adjustable bandgap is offset, however, by difficulties encountered in growing a useful silicon/alloy structure. All semiconductors with lattice spacing close to that of silicon such as gallium phosphide or zinc sulphide are chemically dissimilar and act as dopants to adjacent silicon layers. As well, due to differences in atomic bond structure such a lattice matched alloy grown on a silicon substrate forms islands up to a considerable thickness, making the formation of thin alloy layers difficult. Silicon grown on an alloy substrate, on the other hand, transfers a thin layer of the alloy atoms to the surface for several atomic layers such that a clean interface between the two materials does not form. The solution to the incompatibility of silicon with other lattice matched elements has been to turn to germanium, with a 4.17% larger lattice spacing but similar chemical structure to silicon.

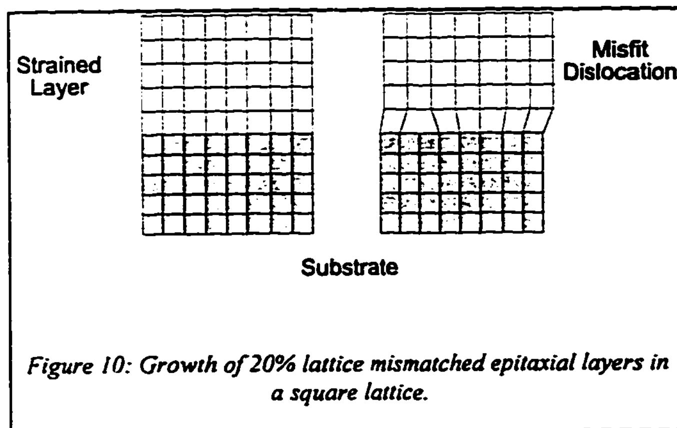

Figure 10: Growth of 20% lattice mismatched epitaxial layers in a square lattice.

The natural growth pattern of silicon germanium on silicon is one of misfit dislocations due to the mismatched lattice spacing, as shown for a simple lattice in Figure 10. Such dislocations introduce disorder into the semiconductor on a large scale. The increase in carrier scattering

resulting from dislocation impurities seriously degrades the heterostructure quality, limiting its use.

'Strained layer epitaxy' refers to the process of growing thin alternating layers of lattice mismatched materials such that the atomic spacings of each shift towards that of the other, replacing misfit dislocations with internal strain as depicted in Figure 10. Pseudomorphic growth of a thin layer of silicon germanium (10-100 atoms thick) on a thick substrate of silicon leaves a stable strained silicon germanium layer matching the smaller lattice spacing of the silicon. As the silicon germanium layer is made thicker or the germanium content is increased the strain is more likely to relax into dislocations, especially as the temperature increases. Strained layers are metastable, and must be kept at low temperatures overall (usually below 600 °C) with only short exposures to higher temperatures (up to 900 °C) to maintain the strain throughout any further growth and processing. Since efficient growth processes have been developed for thermal budgets as low as 550 °C, silicon germanium heterostructures are practical devices to fabricate. Figure 11 shows the 'critical thickness' at which silicon germanium layers grown on silicon relax into dislocations, for a full range of germanium content and a growth temperature of approximately 600 °C.

SiGe Valence Band Structure

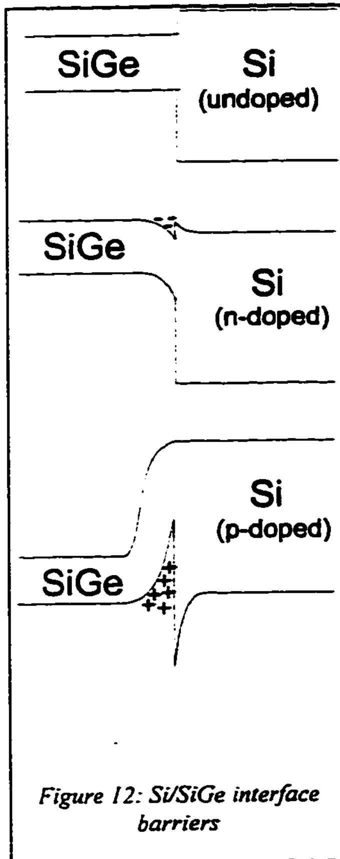

Figure 12: Si/SiGe interface barriers

By varying the fraction of germanium present in the alloy, a range of bandgaps between 0.66-1.12 eV may be achieved. The change in band gap between silicon and an alloy of strained silicon germanium is not evenly divided between the valence and conduction bands, but is biased towards the valence band by a factor of approximately four to one. The large valence barrier makes the Si/SiGe interface most effective for hole confinement, with the formation of a two-dimensional hole gas from p-doped silicon. Figure 12 shows the energy barriers of Si/SiGe interfaces for n, p, and undoped silicon, along with the small electron and large hole confinements made possible by appropriate doping.

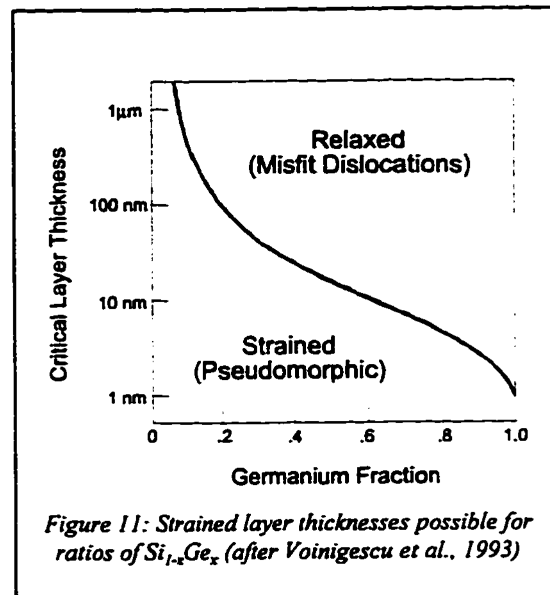

Figure 11: Strained layer thicknesses possible for ratios of $Si_{1-x}Ge_x$ (after Voinigescu et al., 1993)

Valence bands differ from conduction bands in one major way, namely in their asymmetry about the zero wavevector (k=0). Following the split-off of the

third degenerate valence band due to spin-orbit effects, the remaining two valence bands are degenerate at k=0, but have different curvatures corresponding to 'light holes' (LH) with smaller effective mass and 'heavy holes' (HH) with larger effective mass. For silicon germanium, the heavy holes correspond to a total angular momentum quantum number of ±3/2, and the light holes to ±1/2. Although the complexity of the valence band makes it hard to model, it also provides richness to physical phenomena.

The strain of the $Si_{0.87}Ge_{0.13}$ alloy perpendicular to the surface of the alloy layer lifts the degeneracy of the valence band levels further as the crystalline symmetry is reduced. The light and heavy hole bands are split apart at k=0, such that the light hole band has a higher energy (as depicted in Figure 13). Notice also the anisotropy introduced by the effects of strain. The specific energy levels involved for silicon germanium 65 Å quantum wells have been modeled (Rego et al, 1996), taking strain and hole splitting into account. The results are shown in Figure 14, with the quantum well centered around 1000 Å on the z axis. The first heavy hole band occurs at an energy about 25 meV lower

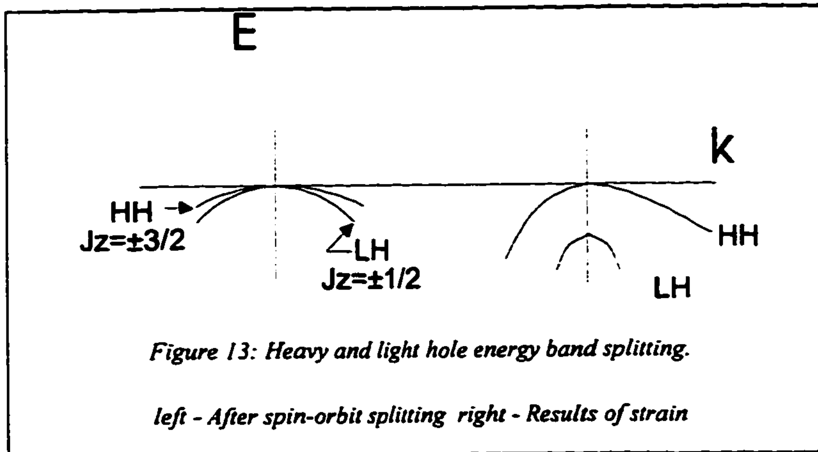

Figure 13: Heavy and light hole energy band splitting.

left - After spin-orbit splitting right - Results of strain

than the next lowest energy level, substantiating the assumption that holes will only populate the lowest heavy hole subband. The fact that the symmetrically doped quantum well preserves inversion symmetry has fundamental consequences in the zero magnetic field properties. This has also been noted in p-type GaAs-AlGaAs quantum wells where large spin-splitting persists down to

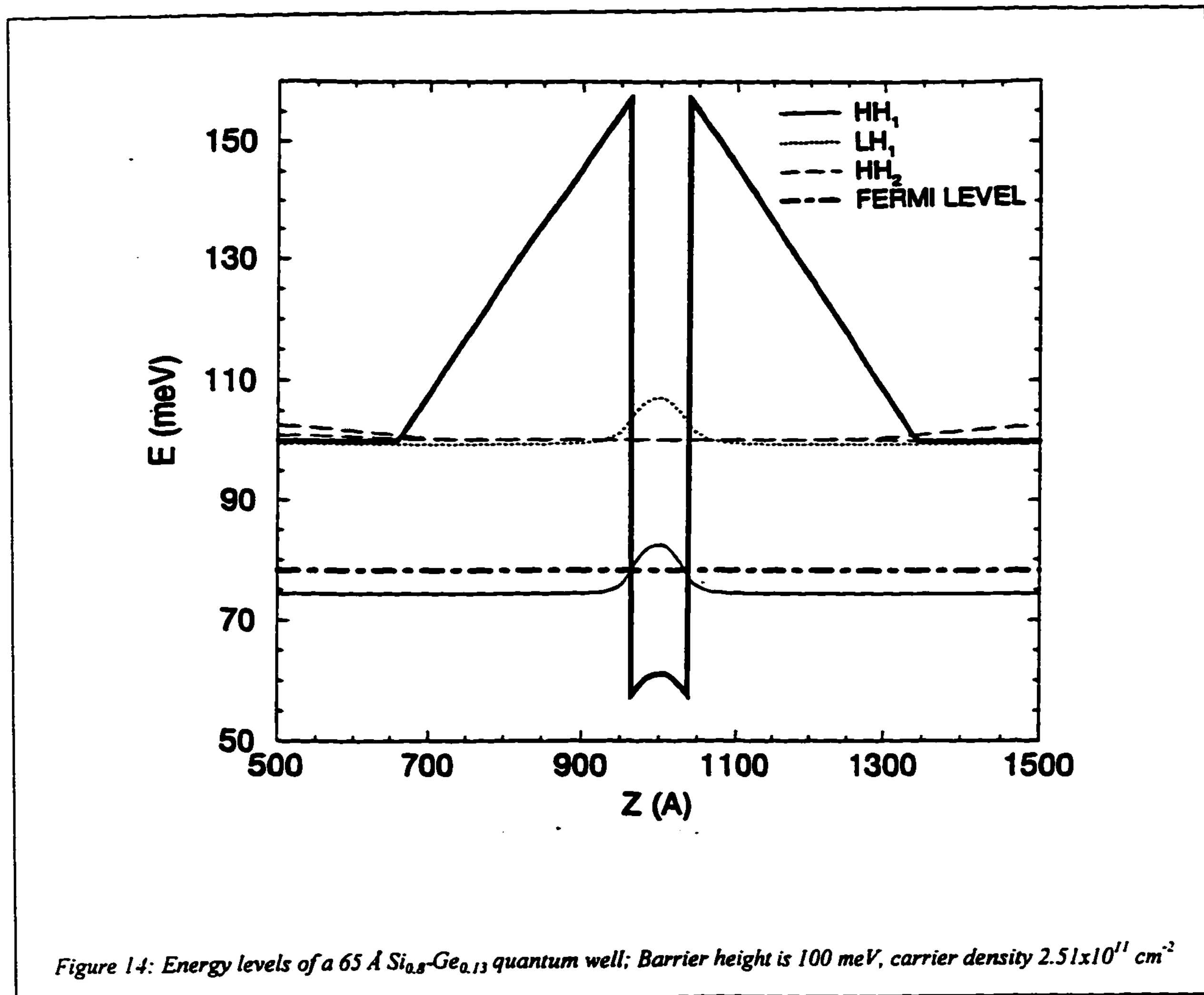

Figure 14: Energy levels of a 65 Å $Si_{0.8}$-$Ge_{0.13}$ quantum well; Barrier height is 100 meV, carrier density $2.51 x 10^{11}$ cm^{-2}

zero field.

SAMPLES AND EXPERIMENTAL DETAILS

Previous work in SiGe quantum wells was carried out on MBE grown samples. Similar samples grown by UHV-CVD (ultra-high vacuum chemical vapor deposition) were found to have a higher mobility. The growth, processing, and characterization techniques will be described in this chapter. The low temperature/high field facility will be discussed, and typical acquisition and analysis of data detailed.

UHV-CVD

All samples were fabricated using ultra-high vacuum chemical vapor deposition (UHV-CVD) by Hugues Lafontaine at the National Research Council Canada. The UHV-CVD technique is used to grow epitaxial layers by streaming reactant gases over a clean wafer surface in carefully regulated quantities resulting in uniform and controllable growth, in this case on (100) silicon wafers at 550°C. Deposition on the silicon wafer surface is an equilibrium process between reactants such as SiH_4, GeH_4 and B_2H_6, and the product H_2. The rate of deposition is a combination of the gas pressures and the temperature of the substrate, both of which may be accurately controlled. Between 550 - 650°C growth rates may be varied in the range of 0.5-10 nm/min, depending in part on the reactant gases being used. The formation of mixed or doped layers simply

300 Å i-Si
500 Å B-doped Si
300 Å i-Si spacer
200 Å $Si_{0.87}Ge_{0.13}$
300 Å i-Si spacer
500 Å B-doped Si
500 Å i-Si buffer
Si (100) -n^-

Figure 15: CVD 124, 200 Å $Si_{0.8}$-$Ge_{0.13}$ quantum well design.

involves mixing the appropriate reactant gases; thus gradual changes in the content of alloys or the doping concentration are not complicated to achieve.

Ultra-high vacuum refers to the partial pressure of water present in the growth atmosphere, which is kept below 10^{-10} mbar. The levels of oxygen and hydrocarbons present are kept even lower, and have been measured using secondary ion mass spectroscopy (SIMS) to be less than 10^{14} cm^{-3}. These contaminant levels are kept low by pumping out the deposition system with the wafers already in place prior to introducing source gases to the reaction chamber. Reactant gases are then introduced up to pressures in the range of 10^{-3} mbar. Preparation of the silicon wafer includes a standard RCA cleaning procedure, which involves a series of chemical baths and deionized water rinses designed to remove all foreign molecules adhering to the surface, while not disturbing the silicon itself. By minimizing contaminants both on the initial substrate and throughout the growth process, uniformity of the grown layers is optimized. The samples described in this work were grown as quantum wells with layer thicknesses as shown in Figure 15 and Figure 16. In both cases the boron doping has a concentration of $1x10^{18}$ cm^{-3}. Sample 124, shown in Figure 15 was designed as a 200 Å symmetrically doped quantum well; samples 32J and 32K shown in Figure 16 are 65 Å quantum wells, almost symmetrically doped. The narrow well width in the latter cases causes the doping asymmetry to be negligible except at very high energy levels which are not energetically available at low temperature.

A temporary layer of silicon oxide was grown on top of the quantum well samples using plasma-enhanced chemical vapor deposition (PECVD). The oxide layer was coated in photoresist which was then exposed with a Hall bar mask over it, and subsequently etched leaving only the Hall bar design. The presence of a protective oxide layer allowed selective etching of the silicon and silicon-germanium layers of the quantum well structure until the Si (100) substrate was reached, at which point the oxide layer was removed and only a Hall bar pattern remained (the Hall bar structure is shown in Figure 17). A 1000 Å thick aluminum layer was deposited on the contact pads of the bar for indiffusion to the 2D layer in the SiGe and subsequent ultrasonic bonding of gold wires.

430/395 Å B-doped Si
300 Å i-Si spacer
65 Å $Si_{0.87}Ge_{0.13}$
300 Å i-Si spacer
500 Å B-doped Si
500 Å i-Si buffer
Si (100) -n^-

Figure 16: CVD 32J/32K 65 Å $Si_{0.8}$-$Ge_{0.13}$ quantum well design.

Schottky Gates

In order to vary the carrier density of the samples examined, Schottky gates were deposited on the main channel and gate contact pad of each sample as indicated in Figure 17. A

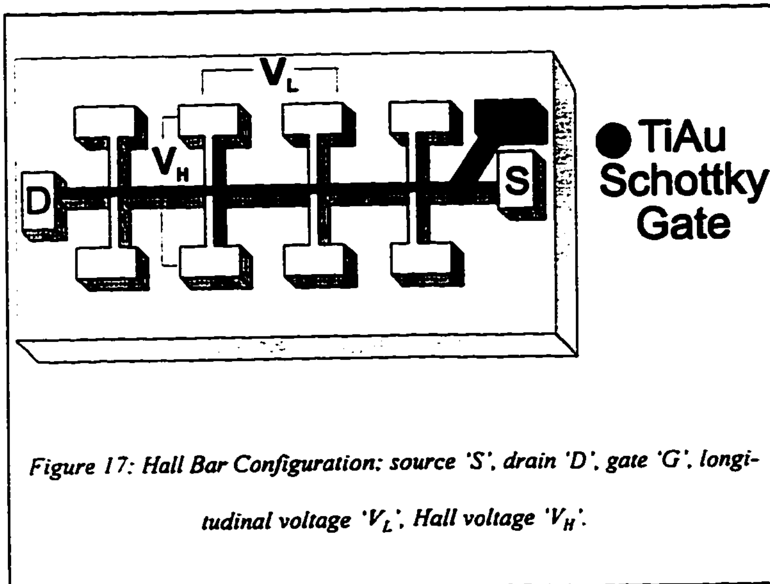

Figure 17: Hall Bar Configuration: source 'S', drain 'D', gate 'G', longitudinal voltage 'V_L', Hall voltage 'V_H'.

Schottky gate consists of a metal layer directly on top of a semiconductor layer, in this case 2000 Å of a titanium-gold alloy (5% Ti, 95% Au) on top of the upper layer of boron-doped silicon. The barrier formed between the two substances is such that a voltage applied to the metal layer will change the carrier density in the quantum well.

The metal-semiconductor junction formed in a Schottky gate is known as a Schottky barrier, and also appears in commonly used Schottky diodes. To form a Schottky barrier with an n-type semiconductor the metal used must have a work function greater than the work function of the semiconductor otherwise a standard ohmic contact will form. When the metal work function is the lower of the two, the resulting potential difference will cause a charge imbalance between the metal and the semiconductor. Carriers in the semiconductor will be pushed away from the surface by the higher density carriers in the metal, balancing the interface dipole layer. A depletion region will form at the semiconductor surface, bending the semiconductor energy bands. As a result the Fermi energies of the two materials will align with an energy barrier at the interface, the height of which is given by the difference between the work function of the metal and the electron affinity of the semiconductor. Figure 18A depicts band bending for a Schottky barrier composed of an n-type semiconductor. Applying a voltage to the metal contact pad of the Schottky gate causes the Fermi level of the semiconductor to separate from that of the metal, and the barrier potential to increase or decrease accordingly as shown in Figure 18B&C.

Some complications do arise in using Schottky gates to change the carrier density of silicon germanium quantum well samples. Schottky gates are difficult to fabricate on silicon surfaces due to the high likelihood of native oxide formation on the bare silicon surface, as well as the presence of surface states which appear even on cleanly cleaved silicon. In order to have a direct contact between the semiconductor and metal gate layer careful surface preparation through cleaning and storage in a vacuum is required, and is often insufficient nonetheless. Schottky gates have even chances of successfully adjusting sample carrier density or failing to do so completely, with functioning gates sometimes only working in a very small range of applied voltages.

The low Schottky barrier height (for all semiconductors) allows some gate leakage when a voltage is applied, regardless of gate design. The smallest leakage values were achieved for sample 32K and were of the order of 10 nA for a gate voltage of 2V. As the gate leakage increases the noise caused by the

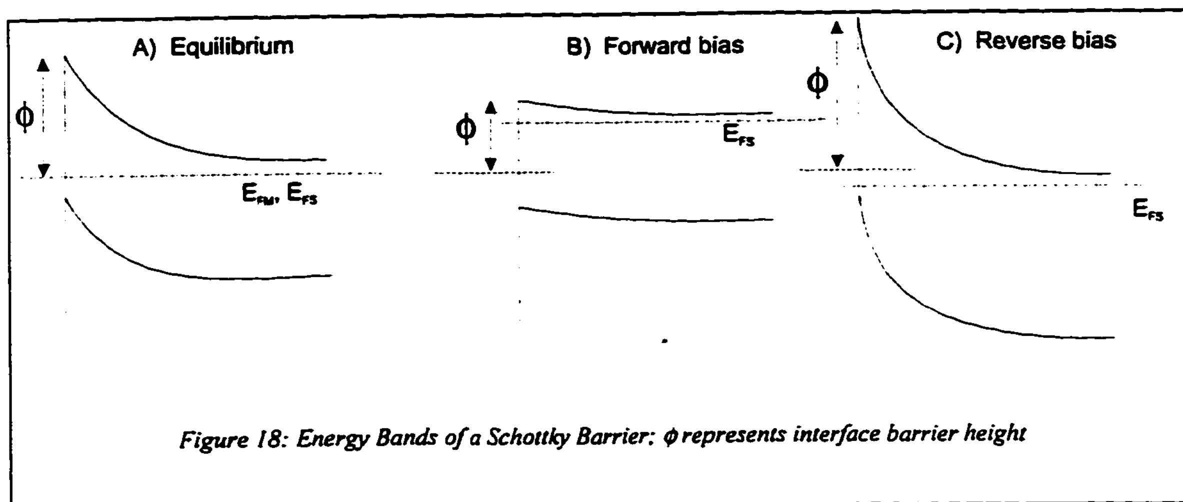

Figure 18: Energy Bands of a Schottky Barrier: ϕ represents interface barrier height

leakage current can disrupt measurements, increasing background noise such that measurements are unstable and obscured. Thus the applied gate voltage must be kept below levels where the gate draws a significant current (100 nA or so), limiting the possible carrier density variation.

Refrigeration

All measurements were performed using an Oxford Instruments top-loading dilution refrigerator, model 400 TLM, at the National Research Council. Such a system allows samples to be warmed and replaced quickly and easily, while the system itself maintains a low temperature (below 2K). The 400 TLM has a cooling power of 400 μW at 100 mK, and a temperature range of 25 mK to 4.2 K. The volume of He^3/He^4 mixture used by the system is 319 gaseous litres in total, with the mixture dumps storing 340 litres. Ideally 31 litres of He^3 are present in a 1:10 ratio with He^4. Changes to the sample temperature in the range of 25 mK to 1.7 K are achieved through heating of the mixture in the sample space using a 500 Ω heater of constantin wire wound inside the base of the mixing chamber. The precise temperature is controlled by a Linear Research LR400 4-wire resistance bridge and a Linear Research LR130 temperature controller in a closed feedback loop mode. The current through the resistor and time constants associated with the heating system may be set manually to optimize the feedback and control. There is also a still heater consisting of a 500 Ω heater of 42 swg constantin wire, controlled by a variable current source in the 0-5 mA range

(made in house). Small still currents are used to create a temperature inversion through the dilution fridge system for efficient cooling.

Samples are mounted on non-magnetic ceramic headers less than 14 mm in diameter and placed at the end of a stainless steel probe through which all external connections for measurement and thermometry run. The wires are arranged in twisted pairs of manganin (for thermometry) or copper (for measurements), with one flexible steel co-axial line for a total of 19 wires. The fully inserted probe places the sample and adjacent thermometers in the dilute phase of the refrigerator for the coldest possible temperature. Thermal anchors are located along the length of the probe at 0.8 K and 4.2 K, with a baffle at 77 K, ensuring good thermal contact with the cryogenic bath. The displacers located between the thermal anchors ensure that a thermal short through formation of a thin film of helium along the probe cannot occur. Two calibrated resistors, one carbon and one ceramic oxynitride, are mounted beside the sample and used to determine the exact temperature for any given measurement. As well, a field independent ruthenium oxide resistor is available for calibration of the other resistors, to record detailed measurements of their magnetic field dependence. The use of magnetic field calibrated multiple sensors with overlapping ranges allows for cross-checking of all measurements and results in accurately determined temperatures. Additional resistors located throughout the refrigerator allow constant monitoring of system performance.

Magnet

The fully inserted sample resides in a glass tail extension of the dilution refrigerator mixing chamber, as shown in Figure 19. The glass tail is located in the base of a 15T Oxford Instruments superconducting magnet, resulting in a vertically oriented magnetic field vector in the sample space. The magnet has an inductance of 170 H, and is formed of inner and outer solenoids made of Nb_3Sn and NbTi wire respectively all held at 4.2K in a helium bath. Full field strength of 15T is reached by ramping the current up to 100A in approximately two hours. A variety of field sweep speeds ranging from 2A/min to 0.01A/min are available to suit the experiment in progress. A manual control system is used for the magnet, and the resulting field is monitored and recorded by the main computer.

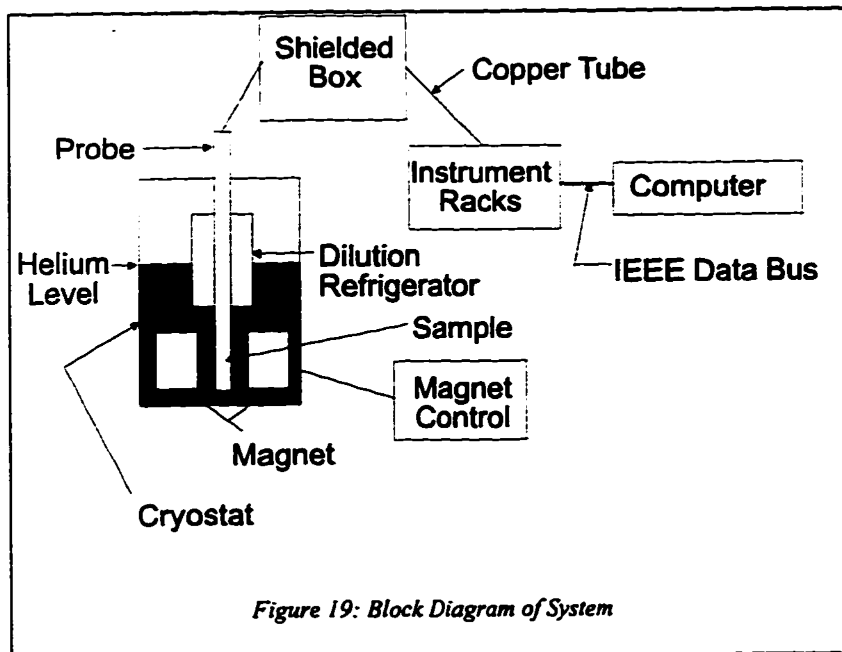

Figure 19: Block Diagram of System

Measurements

From room temperature, grounded samples mounted on the end of the stainless steel probe were cooled over a period of at least three hours with insertion of the probe speeding up once the sample temperature reached 77K.

The gradual cooling process ensured that impurities in the bulk silicon didn't trap electrons (or holes) and create a conduction layer parallel to the two-dimensional hole gas. Samples cooled quickly often have a depleted two-dimensional electron or hole layer which may usually be re-populated while still at low temperature by brief illumination. Slow cooling ensured consistency in the sample state from one warming cycle to the next, and made illumination unnecessary.

In order to reduce background noise in measurements, all signals to and from the probe were sent through a 'shielded box' made of 4 mm thick steel. The shielded box usually housed a battery operated low noise preamp (Stanford Research Systems SR560), a battery operated high impedance amplifier (made in house), and a battery operated voltage source used for the gate voltage bias (also made in house). An accurate current source in the range of pico to microamperes was provided through the use of large high precision resistors again in the shielded box, and a voltage

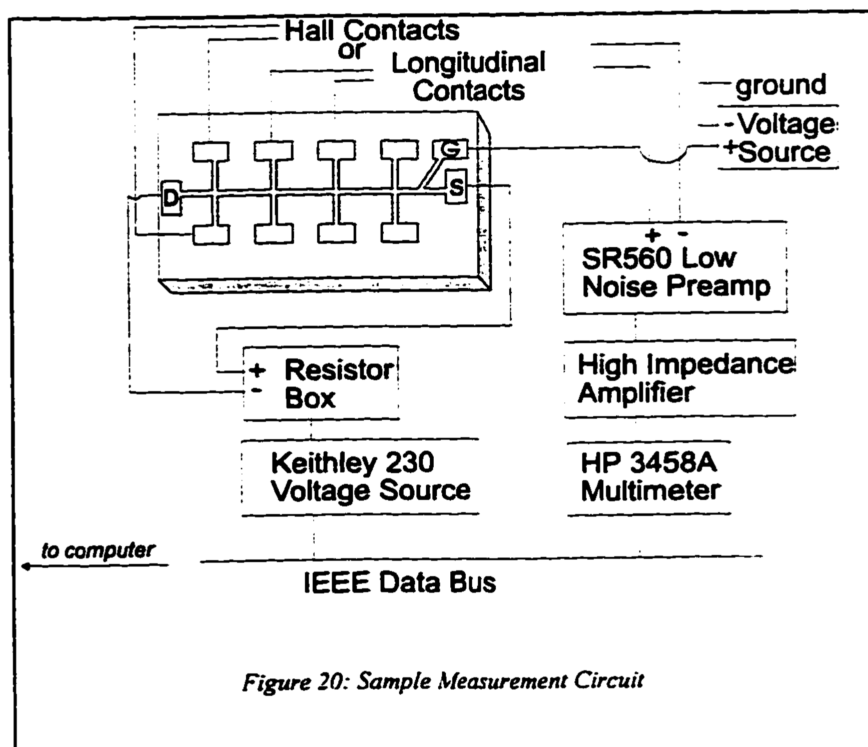

Figure 20: Sample Measurement Circuit

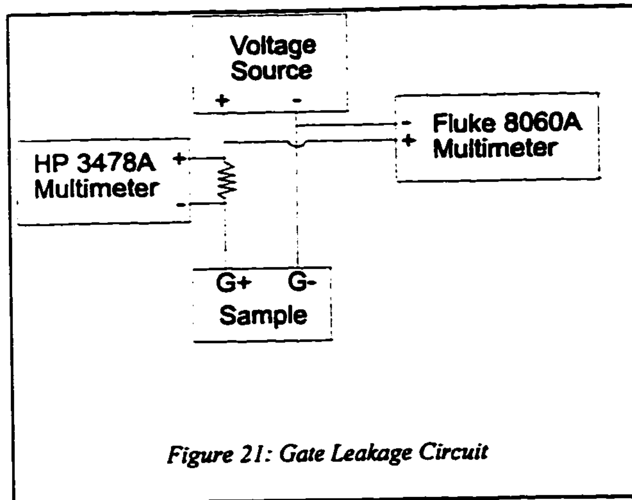

Figure 21: Gate Leakage Circuit

source (Keithley 230) in the equipment racks. Data acquisition was through a 486 PC running LabWindows, connected to each component on the equipment racks by an IEEE data bus, as shown in Figure 20. Changes in sample resistance were measured through the equipment in the shielded box as longitudinal or Hall voltages, with a current flowing across the sample from source to drain, as shown in Figure 17. Measurements of the gate leakage current were made using a sensitive multimeter (Hewlett Packard 3478A) across a large resistor, as shown in Figure 21.

When possible grounded copper tubes housed the long co-axial cables leading from the shielded box to the rest of the equipment, acting as shielding where the wires traverse the varying magnetic field. All equipment in the shielded box was attached to a common ground, linked to the probe, the metal framework supporting the refrigerator, and the copper tubing leading down to the instrument racks. Similarly all equipment on the racks was attached to the same common ground. To avoid interference from ground loops, the ground configuration for the entire system was optimized for each new experiment with the aid of an oscilloscope and a spectrum analyzer.

Sample Design and Characterization

In order to confirm that a two-dimensional system was being studied, the carrier density and the mobility (with no bias on the gate) were plotted as functions of temperature. The result is shown in Figure 22 for the two sample designs considered, along with data from molecular-beam epitaxy (MBE) samples previously established as two-dimensional systems (D'Iorio et al, 1995). The leveling off in both mobility and density as temperature decreases indicates that two-dimensional confinement has been achieved.

The CVD process produced samples of consistently high quality, as is shown in the clarity and magnitude of the Shubnikov-de Haas oscillations in the plot of ρ_{xx} and ρ_{xy} against magnetic field (Figure 23) for sample CVD 124. The same plot also shows the metallic behavior of the sample, evident in the large number of oscillations of approximately the same amplitude in the measurement of ρ_{xx}. The mobility of sample CVD 124 was found by plotting the Landau level filling factors ν (labeled in the figure) against in-

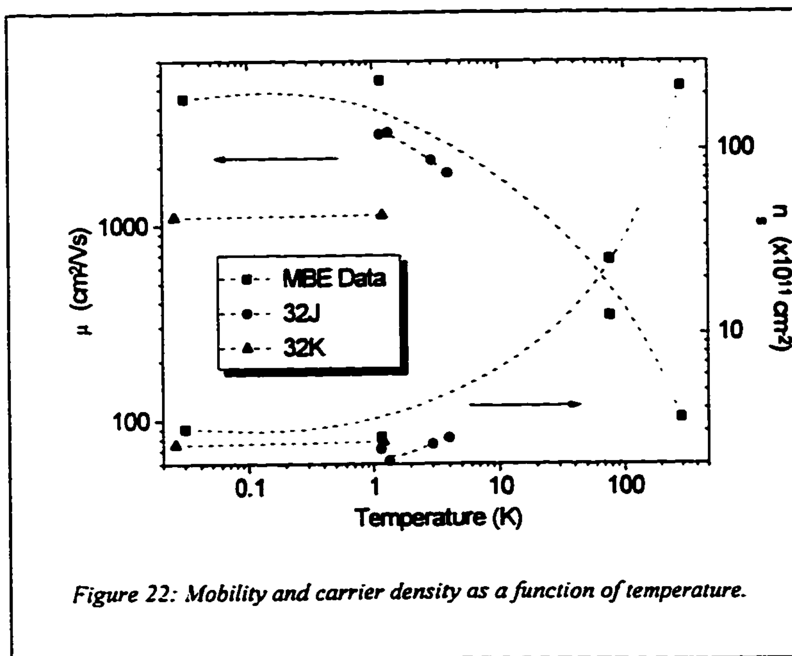

Figure 22: Mobility and carrier density as a function of temperature.

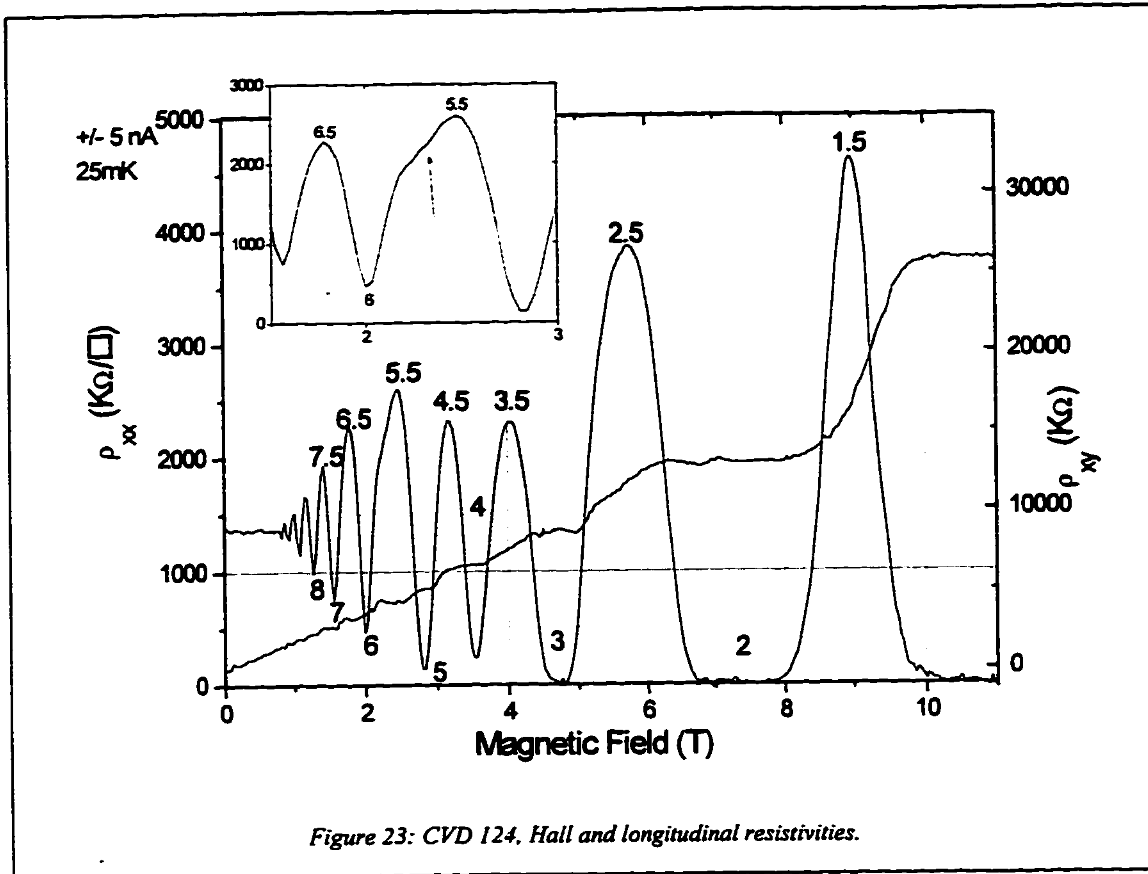

Figure 23: CVD 124, Hall and longitudinal resistivities.

verse magnetic field. From the relationship:

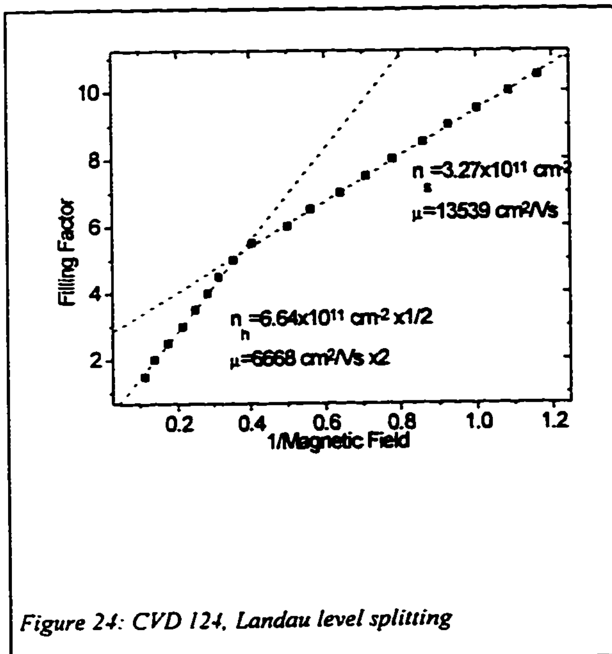

Figure 24: CVD 124, Landau level splitting

2-1 $$\nu = \frac{n_s}{2\frac{e}{h}} \frac{1}{B}$$ where

$$\frac{e}{h} = 2.418 \times 10^{10} cm^{-2} T^{-1}$$

the carrier density with no applied gate voltage was found to be $3.3\text{x}10^{11}$ cm^{-2}. As is shown in Figure 24, the plot of n vs. 1/B has a slope that abruptly changes by a factor of two.

The filling factors between which this shift occurs are indicated in the inset of Figure 23, where a change in peak spacing is evident. Although spin splitting occurs throughout the range of magnetic fields examined, it is at this point that the magnetic field is large enough to resolve the spin splitting; the carrier density determined from high magnetic fields must be corrected by a factor of two as a result.

From the carrier density and the zero field resistivity the transport mobility may be found through the relation:

2-2
$$\mu_t = \frac{1}{n_s e \rho_{xx}(B=0)}$$

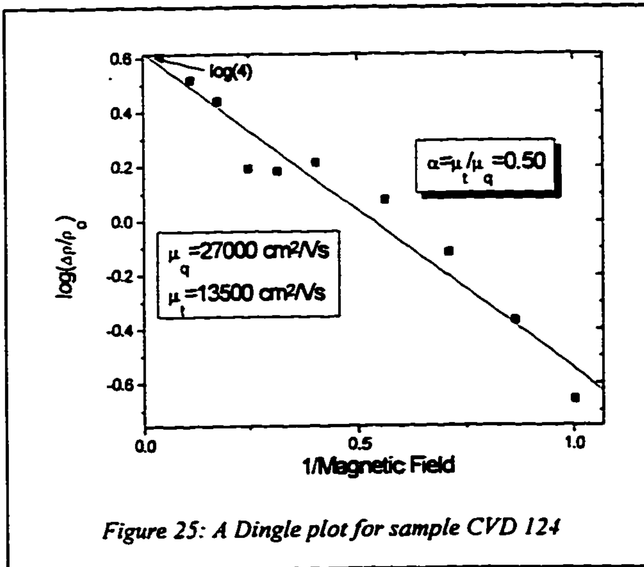

Figure 25: A Dingle plot for sample CVD 124

In the case of CVD 124, μ_q was determined to be 13500 cm^2/Vs with a zero gate voltage. The quantum lifetime may be found from the quantum mobility given the effective mass of the quantum well carriers m*:

2-3
$$\tau_t = \frac{m^* \mu_t}{e}$$

Alternately, if the effective mass is unknown, the following equation may be used to find the effective mass and the quantum mobility:

2-4 $$\log\left(\frac{\Delta\rho_{xx}}{\rho_o}\right) = -\frac{\pi}{\mu_q}\frac{1}{B} + \log\left(\frac{4\xi}{\sinh\xi}\right) \qquad \text{where } \xi = \frac{2\pi m^* kT}{\hbar eB}$$

μ_q may be found from the slope of a plot of $\log(\Delta\rho/\rho_{xx})$ vs. 1/B, and the validity of the relation may be checked through the y-intercept which should equal log(4), as is shown in Figure 25. When the data does not intercept the axis at this point, it is likely that not all mechanisms in play have been taken into account, making the equation invalid as a whole. The effective mass may be found from a plot of $\log(\Delta\rho/\rho_{xx})$ vs $\log(\xi/\sinh(\xi))$, the slope of which should equal one for the appropriate effective mass.

Measurements varying the gate voltage of CVD 124 were less successful, resulting in little to no carrier density variation regardless of the bias voltage applied. Gate leakage measurements of the sample were taken in an effort to determine the cause of the problem. Leakage was in the acceptable range of tens of nanoamperes. The cap layer consisted of 300 Å of intrinsic Si deposited over the doped Si layer, and presumably did not allow for sufficient band bending to affect the carrier density.

Sample 32J was made with a 65 Å quantum well, almost symmetrically doped, as shown in Figure 16. Again a Schottky gate was deposited on top, this time more successfully, with carrier density variation from 2.0-5.8x10^{11} cm^{-2}. The carrier density with no gate voltage applied to the sample was 2.6x10^{11} cm^{-2}. The gate leakage was found to be somewhat larger than that of sample 124 but

still in an acceptable range, as is shown in Figure 26. Sample 32J was found to have an unstable gate in the sense that applying a positive gate voltage caused a permanent change in the state of the gate, and even changed the carrier density at zero bias. As a result, measurements from sample 32J were consistent only within daily data runs, and were not considered conclusive. The sample mobility varied by a factor of two, perhaps as a result of the unpredictable gate behavior. Sample 32J was discarded as its inconsistency became clearly apparent.

Almost identical to sample 32J in design, sample 32K was also fabricated

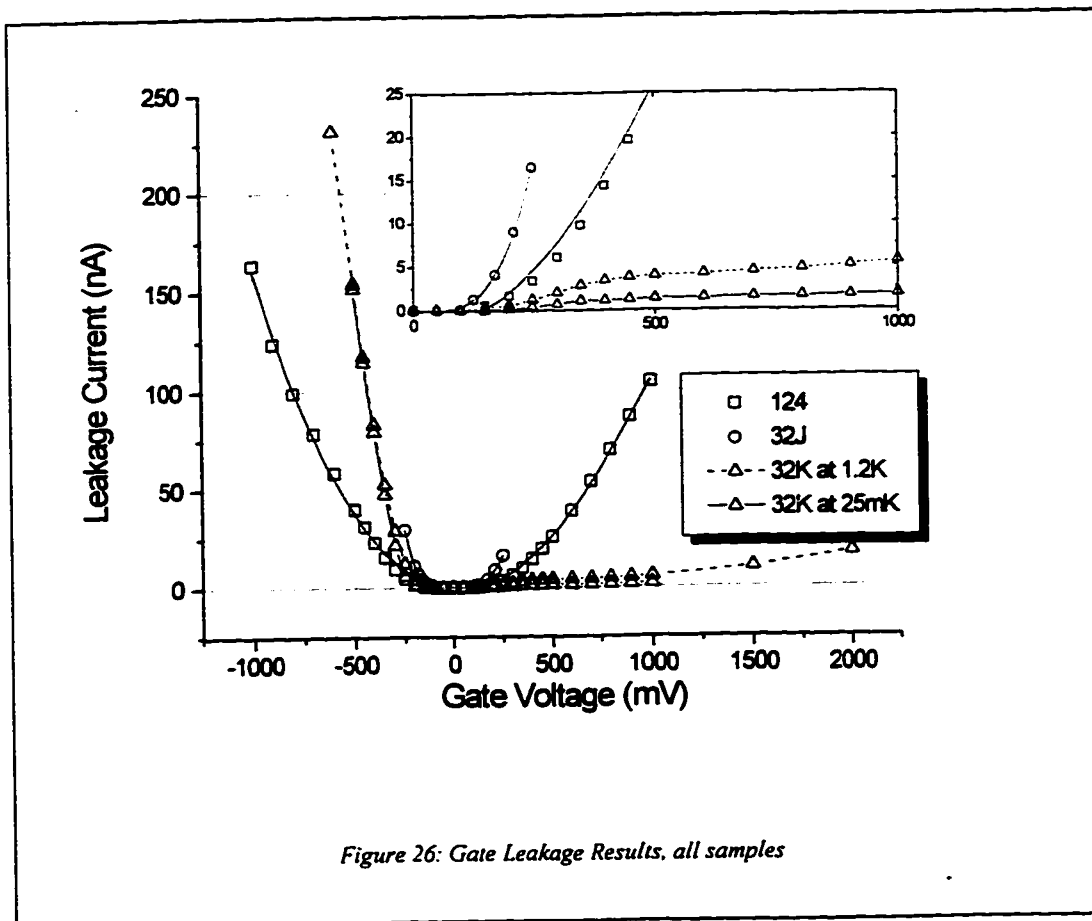

Figure 26: Gate Leakage Results, all samples

with a 65 Å well width but with a top doping layer of 395 Å instead of 430 Å. The Schottky gate deposited on top, however, had a very different leakage pattern. Instead of the near symmetrical leakage seen for positive and negative gate bias in the previous samples, 32K showed almost no leakage for positive bias, and comparably large leakage for negative bias. As well, the small leakage current present at positive gate voltages showed some temperature dependence, while none of the other samples examined showed any change in gate leakage with temperature (in the range of 1.7K to 25 mK).

The lop-sided leakage current suggests that the Schottky barrier is functioning properly, with characteristics similar to a Schottky diode in the reverse bias direction. Repeated measurements over a period of weeks and a range of temperatures and magnetic fields proved sample 32K to have a wide range of reproducible carrier densities, and thus a successful Schottky gate. Carrier density variation in the range of $1.6\text{-}4.3\times10^{11}$ cm^{-2} was achieved over a range of gate voltages between (-300) mV and (+180) mV. In general the gate leakage sets a limit to the carrier variation; in the positive bias range for sample 32K, leakage was low regardless of applied voltage. Instead, high resistivities and concern over the sample's welfare set the limits of the gate voltages used. For sample 32K, the carrier density with no bias applied was found to be 2.6×10^{11} cm^{-2}, while the mobility was 1100 cm^2/Vs.

Despite the difference in gate behavior and carrier density reproducibility between samples 32J and 32K, both exhibited comparable longitudinal resistivities over a range of carrier densities. Those of Sample 32K are shown in Figure 27, with the peak amplitude increasing as carrier density decreases and the sample becomes more insulating.

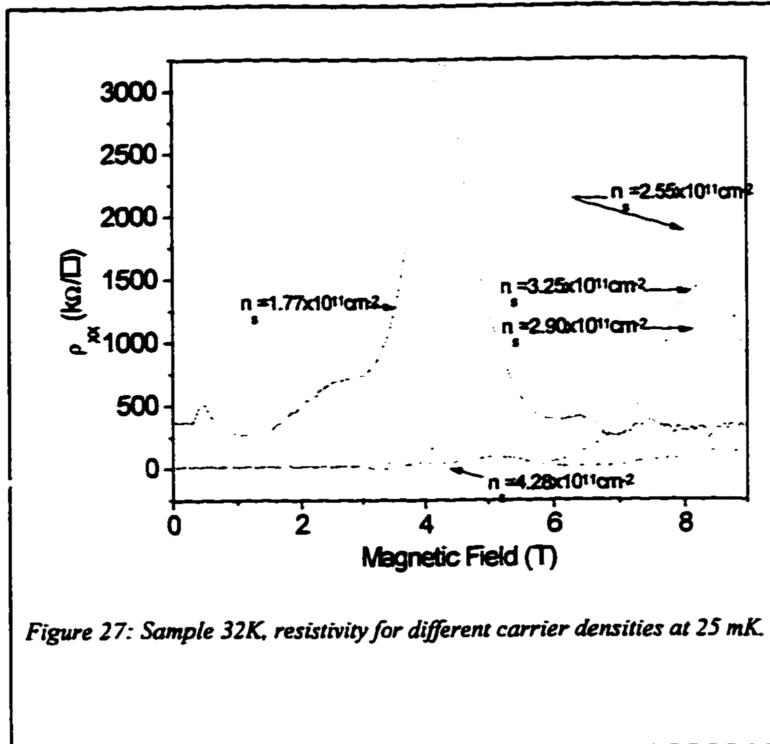

Figure 27: Sample 32K, resistivity for different carrier densities at 25 mK.

In order to determine the type of scattering dominating in each sample, the ratio of transport lifetime to quantum lifetime was found, as is summarized in Figure 28. Long range scattering typically occurs when the ratio α is of the order of ten or more, whereas short range scattering occurs for

	CVD 124	CVD 32J,K
well width	200 Å	65 Å
electron effective mass m*	0.28	0.4
transport mobility μ_t	13500	1100 cm^2/Vs
quantum mobility μ_q	27000	5500 cm^2/Vs
carrier density n	$3.3x10^{11}$ cm^{-2}	$2.6x10^{11}$ cm^{-2}
$\alpha=\tau_t/\tau_q$	0.5	0.2

Figure 28: Sample Characterization Results

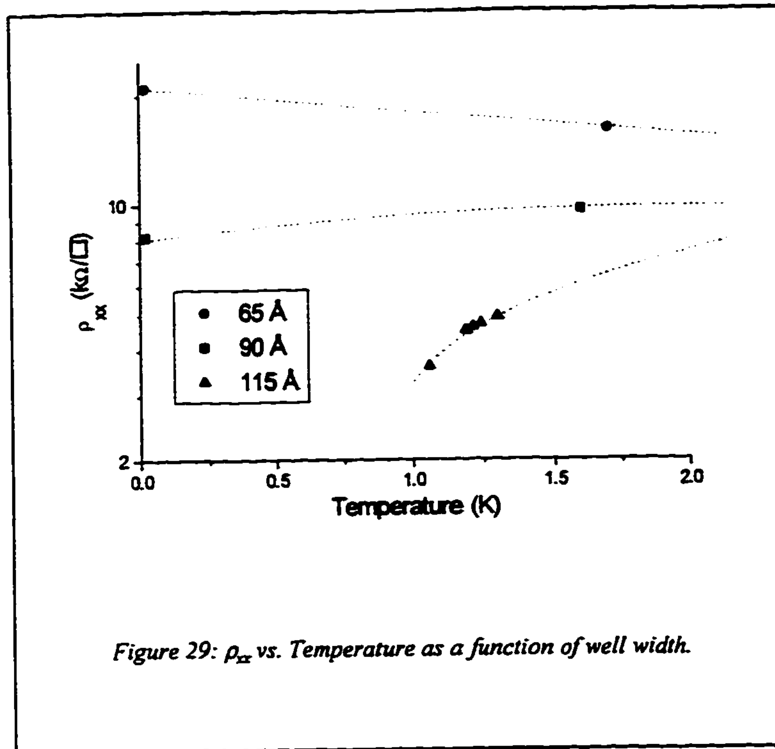

Figure 29: ρ_{xx} *vs. Temperature as a function of well width.*

an α value of the order of one (Das Sarma and Stern, 1985, and Coleridge, 1991). Thus for both samples 32K and 124, short range scattering is dominant.

Previous measurements of SiGe quantum wells suggested that a metal-insulator transition might occur as a function of well width (D'Iorio et al, 1996).· Figure 29 shows measurements made on previous MBE samples without variable carrier density such that the well width is proportional to carrier density; the 115 Å quantum well resistivity shown decreases with temperature as does that of the 90 Å quantum well, suggesting metallic behavior at both well widths. The 65 Å quantum well, however, exhibits an increasing resistivity as temperature decreases and thus appears to be insulating in nature. The well width of 65 Å selected for samples 32K and 32J should result in resistivity values near the metal-insulator transition when no gate voltage is applied, allowing a detailed study of the SiGe metal-insulator transition.

RESULTS AND DISCUSSION

This chapter describes transport measurements at zero magnetic field in symmetrically doped p-type square quantum wells. The motivation for performing such measurements was the indication that a metal-insulator transition was present when results from different samples with varying carrier densities were combined. In addition, such a transition had been shown to occur in high-mobility Si-MOSFETs where the scaling properties suggest a true phase transition at zero magnetic field. One of the SiGe quantum well samples was processed to add a Schottky gate as a top layer and the resistivity at zero magnetic field was then studied as a function of temperature and carrier density. In addition, current-voltage characteristics were studied as a function of temperature and carrier density.. The experimental data will be presented first with the appropriate analysis and the results will be cast in the framework of existing single-particle and collective excitation models.

For a detailed examination of the metal-insulator transition in silicon germanium quantum wells, measurements of the longitudinal resistivity were taken at different temperatures over a range of carrier densities set by adjusting the Schottky gate bias. Unless specified, the error on the data points is estimated to be the size of the point or smaller. The results of the most comprehensive measurements taken from sample 32K are shown in Figure 30A, for the carrier density range of $1.6\text{-}4.3\times10^{11}$ cm^{-2}. As the temperature decreases the sample resistivity

diverges, with lower carrier density measurements showing a large increase in resistivity and higher carrier density measurements a gentle decrease in resistivity.

Figure 30B expands the view of the transition region, clearly showing the metallic nature (resistivity decreasing with temperature) of the high carrier density phase. The top curve is characteristic of insulating behavior (resistivity increasing with decreasing temperature) , while the second from the top oscillates between the metallic and insulating phases, indicating the location of the transi-

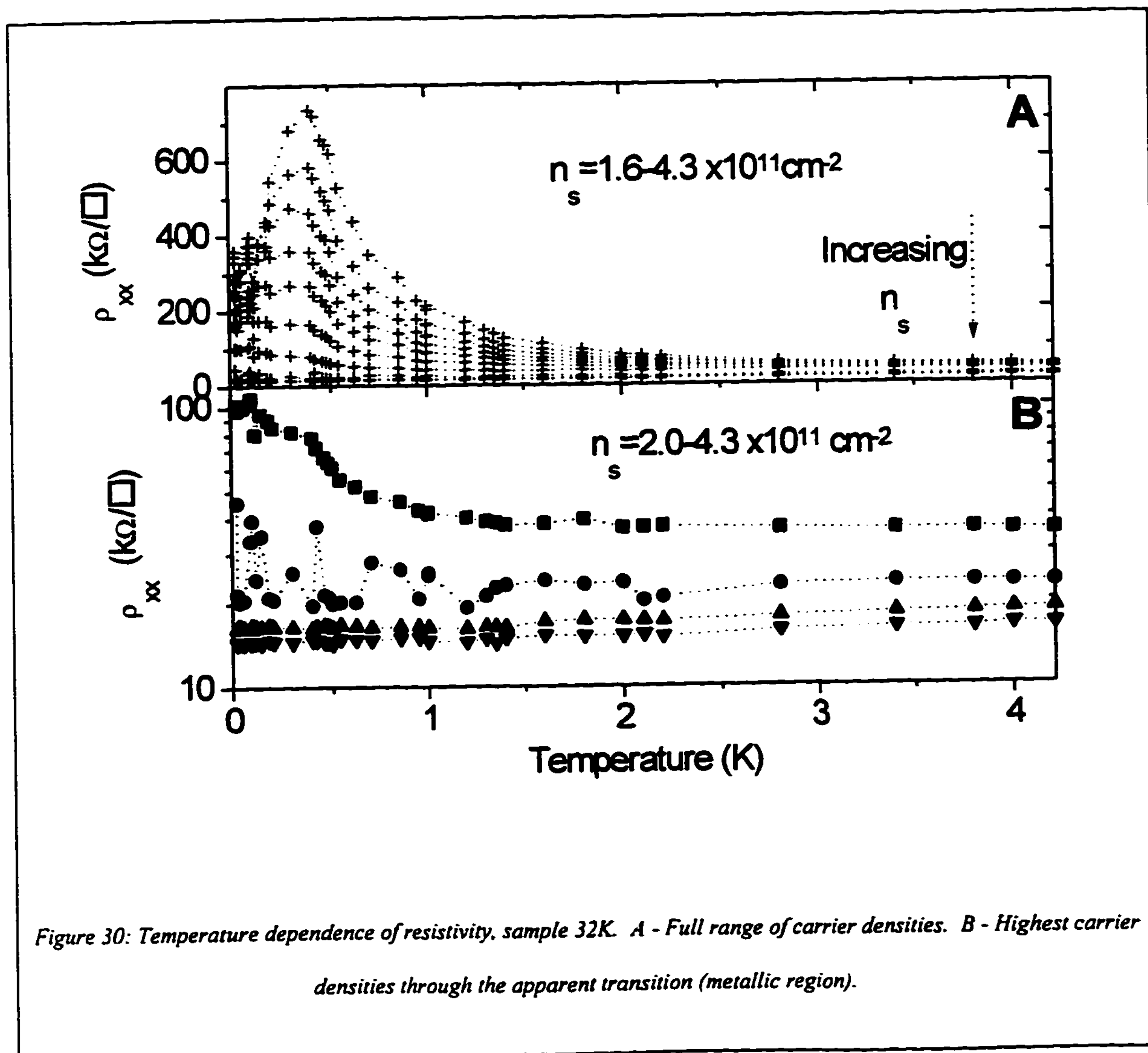

Figure 30: Temperature dependence of resistivity, sample 32K. A - Full range of carrier densities. B - Highest carrier densities through the apparent transition (metallic region).

tion boundary. The expected insulating and metallic phases are present down to a temperature of 400 mK, at which point another transition occurs.

While the insulating and transitional regions resemble those observed in the Si-SiO_2 2D electron system, there is no anomalous decrease of the resistivity in the metallic phase below 1-2 K. In fact, in an ordinary metal one would expect to see a saturation of the resistivity when the phonon frequency Θ becomes less than the inverse elastic scattering time τ^{-1}:

3-1 $$T \leq T_\Theta = h/k_B T$$ (Kravchenko et al., 1995).

In this case the phonon cut-off temperature is of the order of 10 K and the smooth variation of the resistivity in the metallic phase is as expected.

Coulomb Gap

At temperatures between 500 mK and 4.2 K, all of the insulating curves of sample 32K appear to be increasing exponentially. Figure 31 shows the fit for each curve to the Coulomb gap conduction equation (eqn. 1-27):

3-2 $$\rho_{xx} = A \exp\left(\frac{T_o}{T}\right)^Z$$ where T_o is a scaling parameter.

The best fits for the variable Z yielded values between Z=0.4 and Z=0.8, with a mean value of Z=0.5, consistent with the existence of a Coulomb gap. The results span more than one order of magnitude in resistivity. At low temperature, a weaker temperature dependence is observed as the carrier density is in-

creased. The data is consistent with a temperature independent prefactor A where A is close to h/e^2. The prefactor decreases with decreasing density as was observed in high mobility Si-MOSFETs.

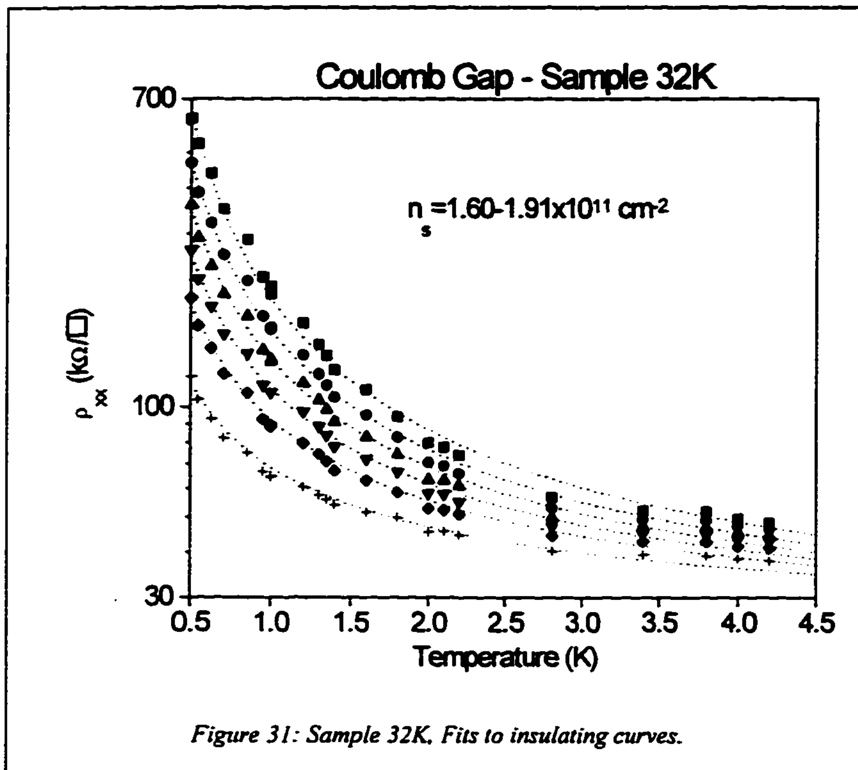

Figure 31: Sample 32K. Fits to insulating curves.

Figure 31 shows a close fit of the Coulomb gap conduction equation for a temperature range of 0.5-2.0 K, with deviations appearing above 2.0 K. The temperature dependence for carrier densities greater than 1.91×10^{11} cm^{-2} becomes activated with:

$$\rho_{xx} \propto e^{\Delta/2k_BT} \qquad (3\text{-}3)$$

where Δ/2 is the activation energy. The data did not fit a variable range hopping conduction mechanism characterized by Z=1/3; this is typical of regimes dominated by single-particle localization. The fit to the Coulomb gap is consistent with the fact that p-type SiGe quantum wells are characterized by strong Coulomb interaction.

Scaling

A universal characteristic of phase transitions is the scaling of the data based on some physical parameter, as was described earlier. In this case the T_o in the Coulomb Gap conduction equation was chosen as a suitable scaling parameter, following the example of Kravchenko et al. (1995). $T_o^{(1)}$ from the most insulating curve (with the lowest carrier density) was used to scale all subsequent curves such that $T_o^{(i)}=\gamma^{(i)}T_o^{(1)}$. Thus all the data was scaled by the factor $\gamma^{(i)}$ to coincide with that for the lowest carrier density. The resulting collapsed plot is shown in Figure 32, with each carrier density represented by a different symbol on the plot. The scaling parameter T_o may be related to the localization length of the sample ξ by equating the thermal energy to the Coulomb interaction, as is justified by Coulomb gap conduction:

3-4 $$k_B T_o = \frac{e^2}{\varepsilon\xi}$$

where $\frac{e^2}{k_B\varepsilon}$ is constant such that the localization length can be derived from the value of T_o. The localization length increases with increasing density. A typical value of ξ in the regime where the Coulomb gap mechanism fits the data well is 10 μm.

The relationship of the scaling parameter T_o with the carrier density then becomes:

3-5 $$T_o(\delta_n) = C|\delta_n|^\beta$$

where $\delta_n = n_s - n_c$, and n_c is the critical carrier density at which the metal-insulator transition occurs and β is the critical exponent of the transition.

Although the resolution of resistivity measurements throughout the phase transition left a range of 2.0-3.4x10^{11} cm $^{-2}$ containing the critical carrier density, a value of 2.2x10^{11} cm $^{-2}$ exactly satisfies the power law relationship between T_o and δ_n while all other values of n_c require an additional term. The universal exponent β is then 1.6±0.2, corresponding to the results of a similar scaling analysis of silicon MOSFETs with a silicon 2D layer, and to the theoretical prediction of 1/β=0.6 (Kravchenko et al., 1995). Such a universal scaling result supports the assumption that a true metal-insulator transition is being observed in the silicon germanium quantum wells examined.

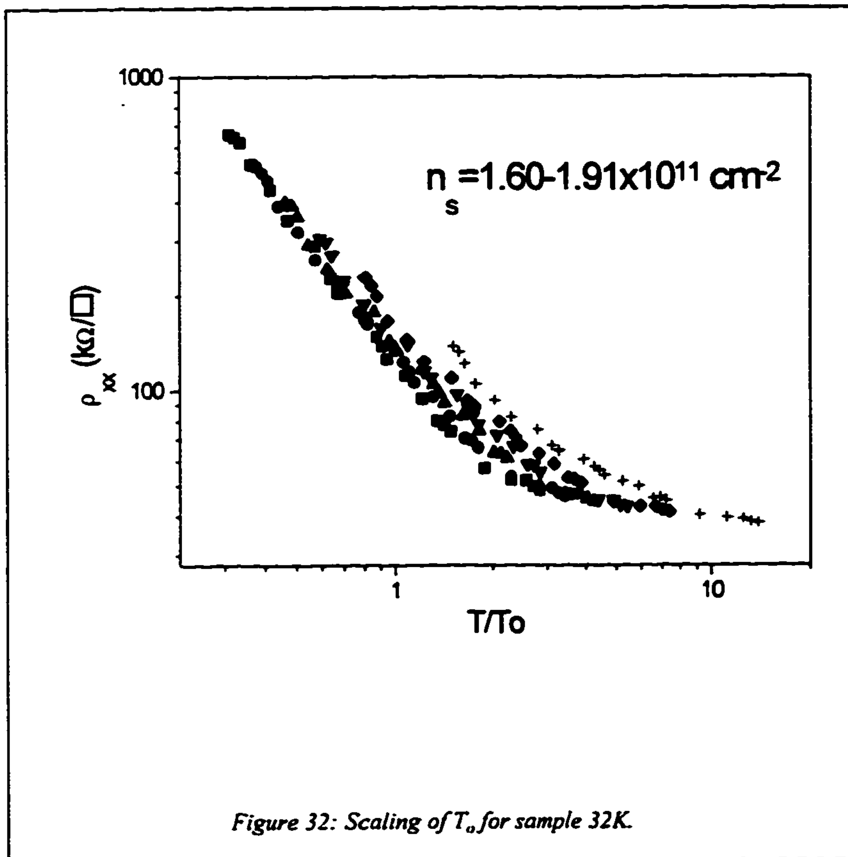

Figure 32: Scaling of T_o for sample 32K.

Kravchenko et al. predicted a breakdown of the scaling as temperature goes to zero and the conduction mechanism switches from the Coulomb gap to variable range hopping. Variable range hopping would be exhibited as a change in the temperature dependence of the resistivity, from $\exp(T_0/T)^{1/2}$ to $\exp(T_0/T)^{1/3}$ (eqn. 3-2). The scaling diagram does show a deviation from a Coulomb gap behavior although a variable range hopping regime is not clearly established.

Low Temperatures

An unexpected change in resistivity occurred as the temperature was decreased below 400 mK, as is evident in Figure 33. Below 400 mK, the insulating behavior at low carrier densities deviates from Coulomb gap transport with resistivity falling for lower carrier densities and rising for higher carrier densities. At approximately 110 mK the resistivity goes through a dip or minimum, recovers slightly and gradually decreases with decreasing temperature. The observed change in the insulating

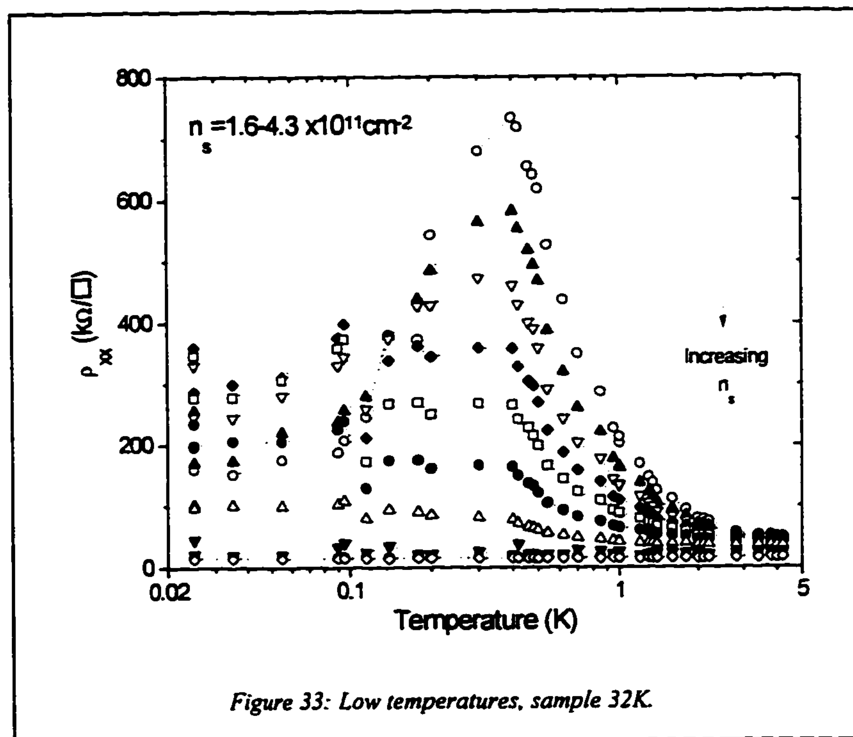

Figure 33: Low temperatures, sample 32K.

phase of silicon germanium is unexpected since this drop in resistivity suggests that delocalization of holes is taking place below 400 mK. It is important to note that the sample resistivity is still quite high, in the order of hundreds of kΩ/□.

Measurements of the resistivity as a function of carrier density are plotted in Figure 34, with each curve representing a different sample temperature. The highest temperature shown (300 mK) has a clearly rising resistivity as carrier density decreases, and subsequent temperatures show the resistivity leveling out for lower carrier densities. The measurements for a temperature of 115 mK are the closest to the critical temperature observed around 110 mK, and show an overall drop in resistivity when compared to both higher and lower temperatures. Finally, measurements taken below the critical temperature exhibit decreasing resistivity with carrier density, and thus de-localization of carriers in the sample.

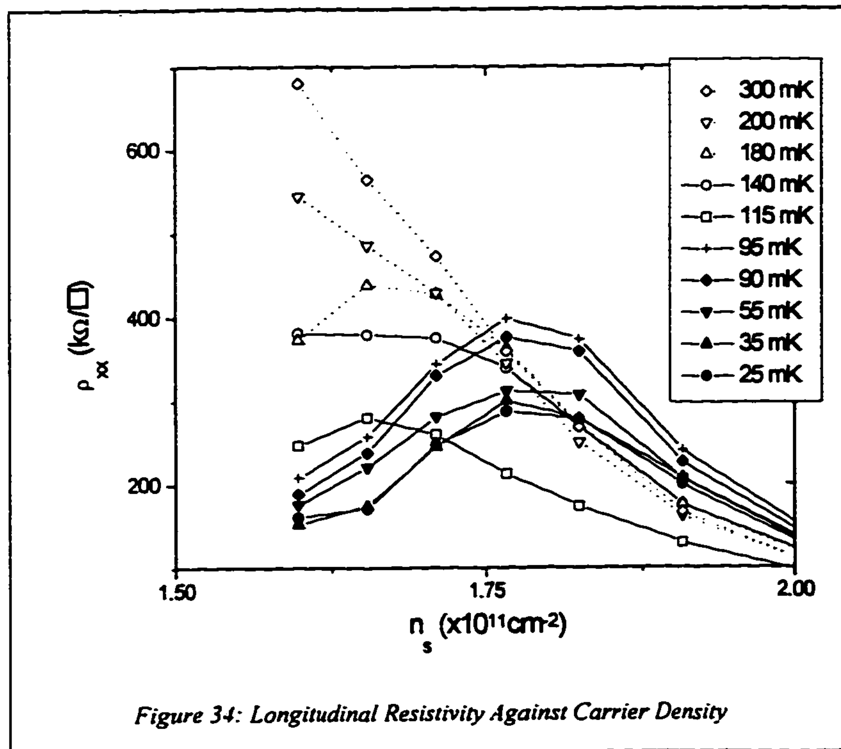

Figure 34: Longitudinal Resistivity Against Carrier Density

All of these changes in resistivity occur at and below a critical carrier density of approximately 1.8×10^{11} cm^{-2}, above

which only a slight drop in resistivity for the 115 mK curve is evident. Thus it appears that a critical carrier density comes into play for the low temperature transition, and is considerably lower than that of n_c=2.2x10^{11} cm^{-2}, the critical carrier density observed for the metal-insulator transition. These results are interpreted as being hallmarks of a phase transition with a critical temperature and a critical carrier density. What leads to the sudden delocalization of carriers is not known but certain obvious experimental causes have been ruled out. For example, the resistivity could drop or stay constant if the 2D hole gas is being heated by the application of a source-drain current which is too large. Joule heating was found to be negligible in our measurements with typical dissipated powers at low densities and milliKelvin temperatures of the order of 300 picowatts or less. The largest dissipation of power was of the order of 1 nW, at 1.7 K, and no changes in resistivity were noted when the current was dropped by an order of magnitude. Another possible effect is a coupling between the Schottky gate and the 2D hole gas through variations in the local potential, when the bias applied to the gate is of the same order of magnitude as the voltage drop measured along the sample. With the gate bias not exceeding 200 mV, such effects could not be observed as the typical potential drop along the sample was of the order of 10 mV or less.

Threshold Field

When the current-voltage relationship is non-linear, symmetry about zero of both variables is usually observed with a single slope apparent in the linear

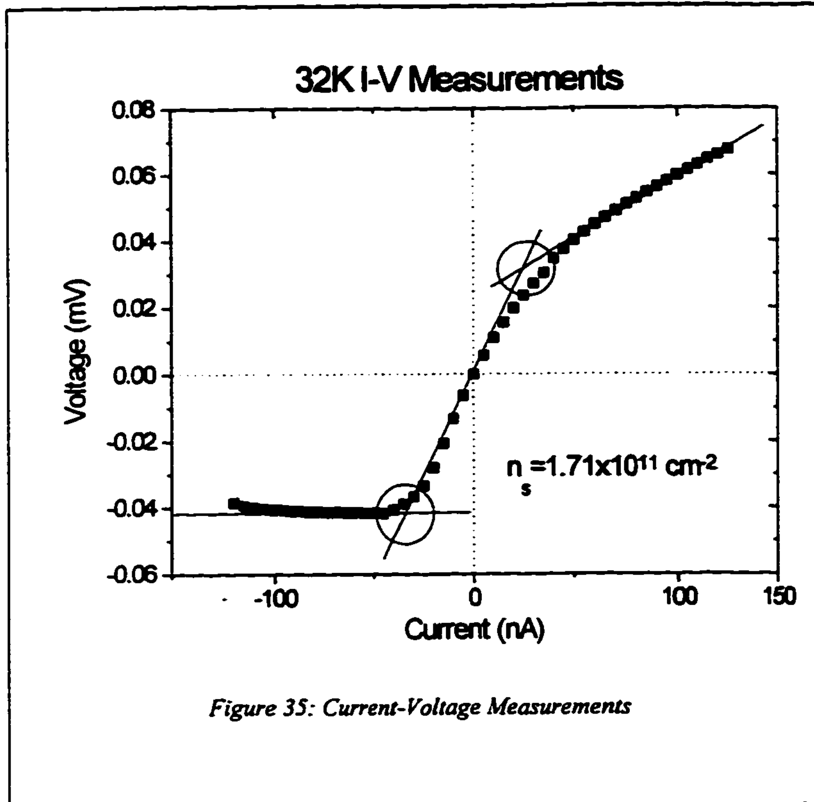

Figure 35: Current-Voltage Measurements

region near zero current and voltage. A threshold voltage may be then measured as the voltage at which the transitional slope appears in either the positive or negative direction. Measurements of current and voltage were undertaken along the length of the sample using four different contacts (including the source and drain). A typical four-wire I-V curve for a carrier density of 1.71×10^{11} cm^{-2} and temperature of 1.7 K is shown in Figure 35. Although the current-voltage characteristic goes through zero voltage and current, it is clearly asymmetric in shape with respect to positive and negative currents. This was also observed for different potential contacts.

The threshold voltage was determined by taking the intercept of the slopes drawn through the central and wing regions of the I-V curve. The absolute values of the circled points were averaged and taken as the threshold voltage. Above 150 nA, current saturation problems made measurements impossible. Attempts to measure the threshold of the second phase, indicated by the

presence of a second slope in the transition region (at higher currents and voltages than the first) proved impossible for all but the most dilute carrier densities. The current-voltage characteristic becomes increasingly linear as the temperature is increased and cannot be attributed to a Joule heating effect as discussed in the previous section.

In order to determine the underlying phenomenon of the non-linear current-voltage characteristic, it is useful to determine the threshold field E_t :

3-6 $$E_t = \frac{V_t}{l}$$ where l is the distance between the sample contacts used for voltage measurements, 400 μm in this case. The result is plotted against δ_n, the difference between the actual carrier density and the critical carrier density of the transition. (Figure 36)

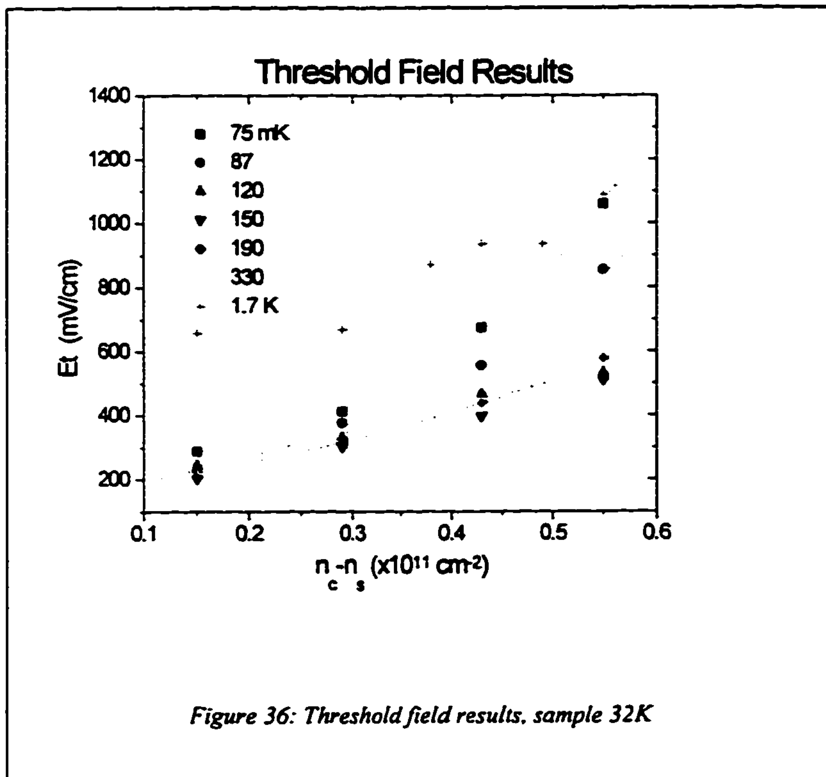

Figure 36: Threshold field results, sample 32K

A fit of the data plotted was undertaken, using the relation: $E_t \propto (\delta_n)^x$ where the exponent x=3/2 has been associated with a pinned

Wigner crystal. There was insufficient data to draw firm conclusions, with the best fit values of the exponent x ranging from 1.0 to 2.6. It is clear from the data shown, however, that a transition of some sort occurs between the 87 mK and 120 mK measurements, corresponding to the observed critical temperature of 110 mK. The lowest temperatures plotted (75 mK and 87 mK) have a threshold field which rises exponentially with δ_n. From 120 mK onwards, the threshold field appears almost linearly related to δ_n. No large increases in threshold field accompany the transition.

A number of features in the threshold field data are noteworthy:

- At 1.7 K the threshold field is large, 600 mV/cm which is typical of a transition to single-particle localization. In that temperature range the I-V curves become linear at high carrier densities.
- Below 110 mK the threshold field near the critical carrier density is of the order of 300 mV/cm and increases exponentially with decreasing density. This is indicative of a crossover to single-particle localization as is expected in the dilute regime when the number of impurities become comparable to the number of carriers.
- In the temperature range of 115-330 mK, the threshold field varies slowly from 200 mV/cm. The magnitude of the threshold field is about a factor of three larger than that observed in high-mobility Si-MOSFETs which is not surprising given that the disorder is larger in the SiGe quantum well samples. The be-

havior of the threshold field as a function of temperature and carrier density is indicative of a phase transition as was revealed in the mapping of the resistivity as a function of the same parameters.

These phase transitions can be studied in the framework of either single-particle or collective excitations of the 2D hole gas. The motivation for studying the resistivity at zero magnetic field was the observation of re-entrant transitions from an insulating state at half-filled Landau levels to quantum Hall effect minima. This same phenomenon had been observed in very high mobility Si-MOSFETs and attributed to the formation of a Wigner solid. At the time, the very high mobility Si-MOSFETs were the only material system with low dielectric constant, large effective mass and little disorder to make Wigner crystallization energetically favorable in the quantum regime at low magnetic fields re-entrant with the quantum Hall effect and at zero magnetic field in the dilute regime as was originally predicted by Wigner. In GaAs-AlGaAs heterostructures, the magnetic field is used to localize the motion of the electrons on small cyclotron orbits until the Coulomb interaction can force the crystallization to occur. This is necessary as the effective mass is small and the dielectric constant is large , making crystallization impossible at zero magnetic field for the usual carrier density range 10^{10} -10^{11} cm^{-2} . What also distinguishes high mobility Si-MOSFETs are the lifting of the valley degeneracy , and the strong spin-orbit coupling. Both the valley and the spin splitting are large at zero magnetic field. These are believed to lead to an enhancement of the Wigner crystallization as in coupled electron gas sys-

tems. It was shown that the presence of pinning impurities acted as a 'seed' for Wigner crystallization. Under what conditions could Wigner crystallization be observed in SiGe quantum wells? A comparative table of energy scales important for crystallization in the quantum regime was presented in Chapter 1 (Figure 8) and shows that given an effective mass twice that of electrons in Si-MOSFETs , p-type quantum wells would be a promising material system to look for a collective excitation such as the Wigner crystallization. Although there is no valley splitting for p-type SiGe quantum wells, it has been shown that the result of mixing of the orbital and spin degrees of freedom in the valence band lead to a replacement of spin by parity as a good quantum number. This effectively results in the 2D hole gas interacting as a coupled hole gas system. This could in principle lead to an enhancement of Wigner crystallization as in the Si-MOSFET situation .

Our results suggest that the 2D hole gas in symmetrically doped quantum wells undergo a series of transitions. As the carrier density is decreased, the temperature dependence of the resistivity reveals that a transition from a metal to an insulator takes place around 2.2×10^{11} cm^{-2}. In the temperature range where the insulating phase fits a Coulomb gap conduction 400 mK - 2 K, the current-voltage characteristics are non-linear and the threshold field near the critical carrier density is consistent with a collective excitation similar to that observed in Si-MOSFETs with a switch over to single-particle localization as the density is decreased. The fact that the threshold field is approximately three times larger in

SiGe would indicate that there is more disorder in this system. The determination of the threshold field is far from ideal given the asymmetry of the current voltage characteristics. However, in samples of comparable density without a Schottky gate, very similar threshold fields were measured with symmetric current-voltage characteristics. If the insulating phase is attributed to the formation of a Wigner crystal, one should think of these as a collection of small crystallites because of the pinning impurities near the interface. The analysis of the quantum and transport lifetimes corroborates the presence of short range scatterers.

The sudden decrease in resistivity between 400 mK and 115 mK followed by a partial recovery and subsequent decrease of the resistivity suggests the occurrence of another transition; two different regimes can be observed in the carrier density dependence of the resistivity (Figure 34). This is also reflected in the density dependence of the threshold field. In the intermediate regime (115-400 mK), the threshold field varies almost linearly. Below 115 mK there is a rapid increase in the threshold field at low densities suggesting a rapid switch over to single-particle localization. It is possible then that the apparent delocalization of carriers or decrease in the resistivity corresponds to a binary phase of the electron gas and the Wigner crystal. The fact that the residual resistivity is still several hundred kilo-ohms supports such a scenario. Although the effect of the gate bias is assumed to be linear in the low density regime it is clear that it becomes impossible to use the Shubnikov-de Haas oscillations to deduce carrier density at the lowest densities. It is possible that the carriers in the dilute regime are not

homogeneously distributed making the formation of a binary phase more probable.

CONCLUSIONS

When the sample characterization was discussed in Chapter 2, it was determined that the scattering in Si-SiGe quantum wells is large angle or short range as reflected by the fact that the ratio of the quantum to the transport life-times is of order unity. This in turn means that the metal-insulator transition at zero temperature and zero magnetic field in a 2D system is no longer forbidden as in Abrahams et al but allowed through the short range scattering potential as predicted by Az'bel. This was experimentally verified in high mobility Si-MOSFETs and accounts for the superconductor-insulator transition in disordered superconducting Bi films (Y.Liu et al, 1991).

The zero field metal-insulator transition in SiGe quantum wells is well established down to 400 mK. As in the Bi films and the Si-MOSFETs, the resistivity in the insulating phase scales with a single parameter T_0 which approaches zero at some critical carrier density n_c and increases as a power $T_0 \propto |n_s - n_c|^{\beta}$ where $\beta = 1.6 \pm 0.2$. The scaling and universality of exponents are hallmarks of a true phase transition. The conduction in the insulating phase is typical of a Coulomb gap. This is consistent with the fact that the hole-hole coupling in p-type SiGe quantum wells is very strong and should be reflected in the conduction mechanism. The metallic phase shows a monotonic decrease of the resistivity with decreasing temperature as would be expected from the phonon cut-off temperature around 10 K. This dependence is very different from that observed in Si-

MOSFETs, where an anomalous drop of the resistivity with no minimum resistivity was observed. The insulating phase is attributed to the formation of a Wigner solid; the non-linear current-voltage characteristics are also suggestive of collective localization.

This work also reveals the existence of another phase transition below 400 mK as seen in the temperature and the carrier density dependence of the resistivity and that of the threshold field. The conduction mechanism at work over the lower temperature transition is not fully understood, and requires further probing. The acquisition of higher resolution resistivity measurements over a suitable temperature range (below 400 mK) would provide valuable insight into the boundaries of the phase transition, conduction mechanism, and perhaps activation energies. As well, cyclotron resonance measurements over the same temperatures would reveal any changes in effective mass related to the transition. The results between 110-400 mK suggest transition to a binary glass-solid phase.

The temperature dependence of the resistivity in the metallic phase is known to vary as a function of the mobility of the sample. This was not studied as part of this work, but leaves open opportunities to explore the effect of different levels of disorder on the observed transitions. With the inevitable appearance of higher quality samples as growth techniques continue to improve, investigation of more insulating regimes may be undertaken. Metal-oxide gates (as opposed to the Schottky gates used in this work) may allow access to a wider range of

carrier densities, but have thus far proven difficult to deposit within the restricted thermal budget.

REFERENCES

E. Abrahams, P.W. Anderson, D.C. Licciardello, and T.V. Ramakrishnan; *Phys. Rev. Lett.*, volume 42, p. 673,1979.

Tsuneya Ando, Alan B. Fowler, and Frank Stern; *Review of Modern Physics*, volume 54, p. 437, 1992

Neil W. Ashcroft, and N. David Mermin; *Solid State Physics*, Holt, Rinehart and Winston, New York, 1976.

Mark Ya Az'bel; *Phys. Rev. B*, volume 45, p. 4208, 1992.

John C. Bean; *Proceedings of the IEEE*, volume 80, p. 571, 1992.

D. Ceperly; Phys. Rev. B, volume 18, p. 3126, 1978.

A.V. Chaplik; *Zh. Eksp. Fiz.* 62, p. 746 [JETP 35, 395], 1972.

P.T. Coleridge; *Phys. Rev. B*, volume 44, p. 3793, 1991.

R.S. Crandall and R.W. Williams; *Phys. Rev. Lett. A*, volume 34, p. 404 , 1971.

S. Das Sarma and F. Stern; *Phys. Rev. B*, volume 32, p. 8442, 1985.

G. Deville; J. Low Temp. Phys., volume 72, p. 135, 1988.

M. D'Iorio, V.M. Pudalov and S.G. Semenchinsky; *Phys. Rev. B*, volume 46,p. 992 , 1992.

M. D'Iorio, D. Stewart, D. Brown, J.-P. Noël, and J. Scott-Thomas; *Proceedings of the 22nd International Conference on the Physics of Semiconductors*, D. Lockwood (editor), World Scientific, Singapore, 1995.

M. D'Iorio, D. Stewart, S. Deblois, D. Brown, and J.-P. Noël; *Surface Science*, p. 361, 1996.

M. D'Iorio; *Physics in Canada*, p. 62, March/April 1996.

Robert Eisberg and Robert Resnick; *Quantum Physics*, John Wiley & Sons, New York, 1985 (2nd edition.).

Helmut Fritsche and David Adler (editors); *Localization and Metal-Insulator Transitions*, Plenum Press, New York, 1985

J.E. Furneaux, S.V. Kravchenko, Whitney E. Mason, G.E. Bowker, and V.M. Pudalov; *Phys. Rev. B*, volume 51, p. 17227 , 1995.

F. Gallet, G. Deville, A. Valdes, and F. I. B. Williams; Phys. Rev. Lett., volume 53, p. 588, 1984.

D.C. Glattli, G. Deville, V. Duburcq, F.I.B. Williams, E. Paris, B. Etienne, and E.Y. Andrei; *Surface Science*, p. 229, 1990.

C. C. Grimes, and G. Adams; Phys. Rev. Lett., volume 42, p 795, 1979.

Y. Guldner, J.M. Berroir, J.P. Vieren, M. Voos, I. Sagnes, P.A. Badoz, P. Warren, and D. Dutartre; *Phys. Rev. B*, volume 48, p. 12312, 1993.

E. Kasper (ed.); *Properties of Strained and Relaxed Silicon Germanium*, INSPEC, IEEE, 1995.

S.V Kravchenko, Whitney E. Mason, G.E. Bowker, J.E. Furneaux, V.M. Pudalov, and M. D'Iorio; *Phys. Rev. B*, volume 51, p. 7038 , 1995.

S.V. Kravchenko, J.E. Furneaux, and V.M. Pudalov; *Phys. Rev. B*, volume 49, p. 2250, 1994.

I. V. Kukushkin, V. I. Fal'ko, R. J. Haug, K. von Klitzing, K. Eberl, and K. Tötemayer; Phys. Rev. Lett., volume 72, p. 3594, 1994.

Jiun J. Liou; *Advanced Semiconductor Devices and Modeling*, Artech House, Boston, 1994.

Y. Liu, K.A. McGreer, B. Nease, D.B. Haviland, G. Martinez, J.W. Halley, and A.M. Goldman; *Phys. Rev. Lett.*, volume 67, p. 2968, 1991.

Shang-Keng Ma; *Modern Theory of Critical Phenomena*, W.A. Benjamin., Massachusetts, 1976.

Whitney Mason, S.V. Kravchenko, G.E. Bowker, and J.E. Furneaux; *Phys. Rev. B*, volume 52, p. 7857, 1995.

R. Mehrottra, B. M. Guenin, and A. J. Dahm; Phys. Rev. Lett., volume 68, p. 641, 1982.

Charles Kittel; *Introduction to Solid State Physics*, John Wiley & Sons, Inc.,New York, 1986.

J.F.A. Nijs (editor); *Advanced Silicon & Semiconducting Silicon-Alloy Based Materials and Devices*, Institute of Physics Publishing, Bristol, 1994.

Sidney Perkowitz; *Optical Characterization of Semiconductors*, Academic Press, London, 1993.

Nasser Peyghambarian, Stephan W. Koch, and Andre Mysyrowicz; *Introduction to Semiconductor Optics*, Prentice Hall, New Jersey, 1993.

Richard E. Prange, and Steven J. Girvin (editors); *The Quantum Hall Effect*, Springer-Verlag, New York, 1990.

L.G. Rego, P. Hawrylak, and J.A. Brum; *Sol. State. Com.*(submitted 1997).

E.H. Rhoderick, and R.H. Williams; *Metal-Semiconductor Contacts*, Clarendon Press, Oxford, 1988.

A. S. Rybalko, B. N. Esselson, and Y. Z. Kovdrya; Sov. J. Low Temp. Phys., 5, 450, 1979.

M. B. Santos, Y. W. Suen, M. Shayegan, Y. P. Liu, L. W. Engel, and D. C. Tsui; Phys. Rev. Lett., volume 68, p. 1188, 1992.

M. B. Santos, J. Jo, Y. W. Suen, L. W. Engel, and M. Shayegan; Phys. Rev. B, volume 46, p. 13639, 1992.

K. Seeger; *Semiconductor Physics*, Springer-Verlag, Berlin, 1982.

B.I. Shklovskii, and A.L. Efros; *Electronic Properties of Doped Semiconductors*, Springer-Verlag, Berlin, 1984.

S.M. Sze (editor); High-Speed Semiconductor Devices, John Wiley & Sons Inc., 1990.

B. Tanatar, and D. Ceperly; Phys. Rev. B, volume 39, p. 5005, 1989.

S. Voinigescu, M. Schumacher, K. Iniewski, R. Lisak, and Z. Parpia; *Electron Technology* , volume 26, p. 25, Institute of Electron Technology, Warsaw, 1993.

Claude Weisbuch, and Borge Vinter; *Quantum Semiconductor Structures*, Academic Press, California, 1991.